



Trem2 Deletion Reduces Late-Stage Amyloid Plaque Accumulation, Elevates the A β 42:A β 40 Ratio, and Exacerbates Axonal Dystrophy and Dendritic Spine Loss in the PS2APP Alzheimer's Mouse Model

William J. Meilandt,¹ Hai Ngu,² Alvin Gogineni,³ Guita Lalehzadeh,¹ Seung-Hye Lee,¹ Karpagam Srinivasan,¹ Jose Imperio,¹ Tiffany Wu,¹  Martin Weber,¹ Agatha J. Kruse,³ Kimberly L. Stark,¹ Pamela Chan,⁵ Mandy Kwong,⁵ Zora Modrusan,⁶ Brad A. Friedman,⁴ Justin Elstrott,³ Oded Foreman,² Amy Easton,¹ Morgan Sheng,¹ and  David V. Hansen¹

Departments of ¹Neuroscience, ²Pathology, ³Biomedical Imaging, ⁴Bioinformatics, ⁵Biochemical and Cellular Pharmacology, and ⁶Molecular Biology, Genentech, Inc., South San Francisco, California 94080

TREM2 is an Alzheimer's disease (AD) risk gene expressed in microglia. To study the role of *Trem2* in a mouse model of β -amyloidosis, we compared PS2APP transgenic mice versus PS2APP mice lacking *Trem2* (PS2APP;*Trem2*^{ko}) at ages ranging from 4 to 22 months. Microgliosis was impaired in PS2APP;*Trem2*^{ko} mice, with *Trem2*-deficient microglia showing compromised expression of proliferation/Wnt-related genes and marked accumulation of ApoE. Plaque abundance was elevated in PS2APP;*Trem2*^{ko} females at 6–7 months; but by 12 or 19–22 months of age, it was notably diminished in female and male PS2APP;*Trem2*^{ko} mice, respectively. Across all ages, plaque morphology was more diffuse in PS2APP;*Trem2*^{ko} brains, and the A β 42:A β 40 ratio was elevated. The amount of soluble, fibrillar A β oligomers also increased in PS2APP;*Trem2*^{ko} hippocampi. Associated with these changes, axonal dystrophy was exacerbated from 6 to 7 months onward in PS2APP;*Trem2*^{ko} mice, notwithstanding the reduced plaque load at later ages. PS2APP;*Trem2*^{ko} mice also exhibited more dendritic spine loss around plaque and more neurofilament light chain in CSF. Thus, aggravated neuritic dystrophy is a more consistent outcome of *Trem2* deficiency than amyloid plaque load, suggesting that the microglial packing of A β into dense plaque is an important neuroprotective activity.

Key words: Alzheimer's disease; amyloid plaque; microglia; microgliosis; neuritic dystrophy; TREM2

Significance Statement

Genetic studies indicate that *TREM2* gene mutations confer increased Alzheimer's disease (AD) risk. We studied the effects of *Trem2* deletion in the PS2APP mouse AD model, in which overproduction of A β peptide leads to amyloid plaque formation and associated neuritic dystrophy. Interestingly, neuritic dystrophies were intensified in the brains of *Trem2*-deficient mice, despite these mice displaying reduced plaque accumulation at later ages (12–22 months). Microglial clustering around plaques was impaired, plaques were more diffuse, and the A β 42:A β 40 ratio and amount of soluble, fibrillar A β oligomers were elevated in *Trem2*-deficient brains. These results suggest that the *Trem2*-dependent compaction of A β into dense plaques is a protective microglial activity, limiting the exposure of neurons to toxic A β species.

Introduction

Since the discovery of *TREM2* (triggering receptor expressed on myeloid cells 2) variants as genetic risk factors for Alzheimer's disease (AD) (Guerreiro et al., 2013; Jonsson et al., 2013), TREM2

biology has become a focal point in research efforts to better understand how the innate immune system impacts AD and other neurodegenerative diseases (Jay et al., 2017b; Ulrich et al., 2017; Yeh et al., 2017). However, whether Trem2 exerts protec-

Received Aug. 1, 2019; revised Dec. 8, 2019; accepted Dec. 23, 2019.

Author contributions: W.J.M., K.L.S., J.E., A.E., M.S., and D.V.H. designed research; W.J.M., A.G., G.L., S.-H.L., K.S., J.I., T.W., M.W., A.J.K., P.C., M.K., and Z.M. performed research; W.J.M., H.N., A.G., S.-H.L., P.C., B.A.F., O.F., and D.V.H. analyzed data; W.J.M., H.N., M.W., A.E., M.S., and D.V.H. edited the paper; W.J.M. and D.V.H. wrote the paper; H.N. contributed unpublished reagents/analytic tools; D.V.H. wrote the first draft of the paper.

We thank Melissa Gonzales Edick and Joanna Yung for imaging support; members of the Genentech animal care staff, FACS laboratory, and RNA sequencing laboratory for other research support; and Chris Bohlen for helpful critique of the manuscript.

All authors are or were employees of Genentech, Inc., with interests in developing novel therapeutics for neurodegenerative diseases at the time of performing work for this manuscript.

tive or detrimental functions in mouse models of AD-related neuropathology has been rather unclear (Gratuze et al., 2018; Hansen et al., 2018; Ulland and Colonna, 2018).

In transgenic models of cerebral β -amyloidosis, plaque load has been reportedly increased, decreased, or unchanged in mice that lack Trem2, depending on the model, age, and brain region being analyzed (Jay et al., 2015, 2017a; Wang et al., 2015, 2016; Yuan et al., 2016; Parhizkar et al., 2019). Trem2 deletion in amyloidosis models has also been reported to either increase or decrease phosphorylation of the endogenous tau protein (Jay et al., 2015; Wang et al., 2016). Similarly, studies in neurodegeneration models driven by transgenic expression of the human tau protein have suggested disparate roles of Trem2. In the hTau model (Andorfer et al., 2003), Trem2 deletion increased the amounts of tau phosphorylation and aggregation detected (Bemiller et al., 2017). In contrast, in the PS19 model (Yoshiyama et al., 2007), Trem2 deletion had a protective effect, preventing tau-driven synaptic loss and atrophy in the hippocampus and entorhinal cortex, respectively (Leyns et al., 2017).

Transcriptional profiling studies have defined a disease/damage-associated microglial (DAM) activation state that is commonly observed in the brains of neurodegeneration models (Deczkowska et al., 2018; Friedman et al., 2018). The acquisition of the DAM state is Trem2-dependent in mouse models of AD, amyotrophic lateral sclerosis, and demyelinating disease (Poliani et al., 2015; Wang et al., 2015; Keren-Shaul et al., 2017; Krasemann et al., 2017). Some have argued that this state of microglial activation or alarm is fundamentally protective (Keren-Shaul et al., 2017), whereas others have argued that this state is damaging and that returning microglia to their normal “homeostatic” state would be beneficial (Krasemann et al., 2017). It is conceivable that microglial TREM2 activity may be either protective or detrimental, depending on the disease stage and types of pathology present.

To clarify the role of Trem2 in β -amyloid-driven AD models, we studied the effects of Trem2 deletion on microglial activation, plaque accumulation, and neuronal pathology in the PS2APP model across a wide range of ages and in both sexes. PS2APP mice develop amyloid plaque and attendant gliosis pathologies that increase with age, with female mice accumulating the pathology more rapidly than males (Ozmen et al., 2009). Here we report that the effects of Trem2 deficiency on plaque load varied with age and sex, but notably, plaque accumulation was reduced at older ages in both female and male Trem2 KO (PS2APP; Trem2^{ko}) mice compared with age-matched Trem2 WT (PS2APP; Trem2^{wt}) mice. We consistently observed that the A β 42:A β 40 ratio was elevated, plaque morphology was more diffuse, and neuritic dystrophy histopathology was more marked in PS2APP; Trem2^{ko} mice, even at older ages when total plaque was reduced. Additional analyses of PS2APP; Trem2^{ko} mice at 12 months of age revealed ApoE-laden microglia, increased levels of soluble fibrillar oligomeric A β , and elevated neurofilament-L in the CSF. By RNAseq, we observed that proliferation-related transcripts in PS2APP;

Trem2^{ko} microglia were reduced, particularly those encoding certain components and regulators of Wnt-related signaling. Collectively, our data indicate that Trem2-dependent microglial proliferation and activation attenuate the toxic effects of A β toward neurons (i.e., the DAM state is mainly protective) and that measurements of neuronal pathology are more informative than plaque load as readouts of microglial modulation in models of β -amyloidosis.

Materials and Methods

Animals. All animal care and handling procedures were reviewed and approved by the Genentech Institutional Animal Care and Use Committee and were conducted in full compliance with regulatory statutes, Institutional Animal Care and Use Committee policies, and National Institutes of Health guidelines. Animals were housed in specific pathogen-free conditions with 12 h light/12 h dark/d and maintained on regular chow diets. The Trem2^{tm1(KOMP)V1cg} null allele (C57BL/6N background) was crossed into the PS2APP model (C57BL/6J background). To generate experimental cohorts, all breeding mice were homozygous carriers of the PS2APP transgene and heterozygous carriers of the Trem2-null allele to allow maximal use of littermates between Trem2 WT (Trem2^{wt}) and Trem2 KO (Trem2^{ko}) PS2APP groups. We designed our study to analyze female cohorts at early (4 months), intermediate (6–7 months), and late (12 months) stages of pathology. We also analyzed males at the age of 6–7 months, a common age for us to examine PS2APP histopathology, to check whether any observed effects of Trem2 deletion were sex-specific. The 4 and 6–7 month cohorts were processed together; the 12 and 19–22 month cohorts were separate batches. When we observed less plaque in 12 month PS2APP; Trem2^{ko} females, we decided to also analyze their still aging male counterparts to learn whether that effect was reproducible. (By that time, the numbers of aged males were somewhat depleted, so we included available Trem2^{het} mice to round out the analysis.) For dendritic spine analysis, animals also carrying the Thy1:GFP-M transgene (Jackson ImmunoResearch Laboratories, stock #007788) were used.

Flow cytometry and FACS. Animals were anesthetized with ketamine/xylazine and transcardially perfused with 30 ml of ice-cold PBS before dissection of cortex + hippocampus. Care was taken to remove the choroid plexus and as much of the meninges as possible before dissociation and sorting. Tissues were dissociated and cell suspensions prepared as described previously (Srinivasan et al., 2016). All steps were performed on ice or at 4°C to prevent artifactual microglial activation.

For quantifying CD45 immunoreactivity and collecting brain-resident myeloid cells by FACS, cell suspensions from 7 PS2APP; Trem2^{wt} (5 females, 2 males) and 7 PS2APP; Trem2^{ko} (6 females, 1 male) mice at 14–15 months of age were stained with the following antibodies in Hibernate-A medium for 20 min at 4°C on a rotator: APC-conjugated anti-CD11b (BD Biosciences, 561690, 1:200), PE/Cy7-conjugated anti-CD45 (BD Biosciences, 552848, 1:500), FITC-conjugated anti-Ly6g (Tonbo Biosciences, 35-5931, 1:200), and PE-conjugated anti-Ccr2 (R&D Systems, FAB5538P, 1:200). Samples were briefly washed and stained with DAPI before FACS sorting. Myeloid cells were selected by gating live (DAPI-negative) cells for CD11b and CD45 immunoreactivity. To avoid the presence of peripheral myeloid cells in the flow analysis and FACS collections, Ccr2⁺ cells (peripheral monocytes/macrophages) and Ly6g⁺ cells (neutrophils) were excluded. The total population of brain-resident myeloid cells (defined as CD11b⁺CD45⁺Ccr2⁻Ly6g⁻), consisting almost entirely of microglia but including CD45^{high} perivascular macrophages (~2% of total), from each sample was collected in Hibernate-A. Collected cells were pelleted at 5000 rcf for 8 min, and RNA was extracted from cell pellets using QIAGEN RNeasy Micro kits. To measure CD45 immunoreactivity of brain myeloid populations during FACS, CD45^{low} and CD45^{high} gates were defined using a nontransgenic animal as a control to identify microglia in their normal state (CD45^{low}). The same gates were transposed onto cells from PS2APP animals sorted on the same day in the same machine to ensure accuracy and consistency in determining percentages of CD45^{low} and CD45^{high} populations. Generally, animal pairs, including one PS2APP; Trem2^{wt} and one PS2APP; Trem2^{ko} animal, were processed together from perfusion through

Correspondence should be addressed to David V. Hansen at hansen.david@gene.com or William J. Meilandt at meilandt.william@gene.com.

K. Srinivasan's present address: Alector, South San Francisco, CA 94080.

A.J. Kruse's present address: University of Washington, Seattle, WA 98195.

M. Sheng's present address: Broad Institute of Massachusetts Institute of Technology and Harvard, Cambridge, MA 02142.

<https://doi.org/10.1523/JNEUROSCI.1871-19.2019>

Copyright © 2020 Meilandt et al.

This is an open-access article distributed under the terms of the Creative Commons Attribution License Creative Commons Attribution 4.0 International, which permits unrestricted use, distribution and reproduction in any medium provided that the original work is properly attributed.

sorting. Data for nontransgenic animals in Figure 1F include the nontransgenic animals used to define the CD45 gates used during PS2APP cell sorting, as well as additional age-matched control animals from another cohort processed at another time (due to animal availability constraints).

For measuring microglial cells with β -amyloid content, animals at ~12 months ($n = 3$ PS2APP;Trem2^{wt} and 2 PS2APP;Trem2^{ko}) were intraperitoneally injected with methoxy-X04 (10 mg/kg) 24 h before tissue collection. Animals were processed as described above, and dissociated cells were stained for CD11b. Cells were also incubated with Calcein-AM (eBioscience, 65-0853-39, 1:1000) just before flow cytometry to label live cells using the 488 nm excitation channel. Live CD11b⁺ cells were gated as X04⁺ or X04⁻ using the DAPI excitation channel to determine the percentage of microglia with ingested amyloid content. Transgenic animals injected with PBS were also used as negative controls (data not shown).

RNA sequencing, differential expression, and gene set analysis. RNA samples from sorted brain myeloid cells of 7 PS2APP;Trem2^{wt} (5 females, 2 males) and 6 PS2APP;Trem2^{ko} (5 females, 1 male) mice (14–15 months old) were selected for sequencing. The concentration of RNA samples was determined using DS-11 spectrophotometer (DeNovix), and the integrity of RNA was determined by 2100 Bioanalyzer (Agilent Technologies). Approximately 1–5 ng of total RNA was used as an input material for the library generation using SMART-seq v4 Ultra Low Input RNA kit (Clontech). Size of the libraries was confirmed using 4200 TapeStation and High Sensitivity D1K screen tape (Agilent Technologies), and their concentration was determined by qPCR-based method using KAPA Library Quantification Kit. The libraries were multiplexed and then sequenced on HiSeq4000 (Illumina) to generate 30 M of single-end 50 bp reads. Sorted cell RNA-Seq data were analyzed as described previously (Srinivasan et al., 2016). Briefly, Illumina adapters, low-quality sequences, and rRNA reads were first discarded. Remaining reads were aligned to the GRCh38 genome with GSNAP aligner (Wu et al., 2016), and reads overlapping each gene were quantified. Normalization was based on the nRPKM method, which is proportional to size factor normalization of DESeq (Love et al., 2014). Differential expression was performed using voom+limma (Law et al., 2014). Raw RNA-Seq data have been deposited to NCBI GEO under accession number GSE140744.

Heat maps in Figure 2A and Fig. 2-3 (available at <https://doi.org/10.1523/JNEUROSCI.1871-19.2019.f2-3>) were generated using gene sets of interest to compare transcriptional responses in multiple datasets. z scores were calculated as follows. First, log₂-scale expression matrices were calculated as $\max(\log_2(\text{nRPKM}), -4)$. Then, each gene was centered and scaled to give z scores: for a given gene/sample combination, the z score represents distance of nRPKM value in SDs from the mean log₂-scale expression value for that gene across all samples within a dataset. Rows (genes) were organized hierarchically using the Euclidean distance function. Columns (sorted microglia samples) were organized by project and genotype.

Gene ontology (GO) query was submitted on the PANTHER Classification System version 14.1 (Mi et al., 2019) at the website (<http://pantherdb.org/>) using the following inputs: Gene list = genes differentially expressed between Trem2^{ko} and Trem2^{wt} PS2APP microglia (fold change ≥ 2 , adjusted p value ≤ 0.05); Organism = *Mus musculus*; Analysis = statistical overrepresentation test; Annotation set = GO biological process complete; Reference list = *Mus musculus* whole genome genes; Test type = Fisher's exact; Correction = Calculate false discovery rate (FDR).

For gene set enrichment analyses in Figure 2D and Fig. 2-2 (available at <https://doi.org/10.1523/JNEUROSCI.1871-19.2019.f2-2>), each sample was assigned a gene set score using log₂(nRPKM) values for each gene in the set. A sample's gene set score reflected the average difference, for all genes in the set, between that sample's measured log₂(nRPKM) value for a given gene and the average log₂(nRPKM) value for the same gene across all samples. In cases when one or more samples had no transcripts detected for a given gene, an imputed log₂(nRPKM) value was assigned equal to one log₂ step below the lowest log₂(nRPKM) value detected for that gene in that sample set. We compared gene set scores between geno-

type groups using two-tailed t tests assuming unequal variance between groups.

Sectioning, histological and immunological staining. Single-sex cohorts of animals used for histological and biochemical analyses included 4 month females ($n = 11$ nontransgenic Trem2^{wt}, 14 nontransgenic Trem2^{ko}, 10 PS2APP;Trem2^{wt}, and 12 PS2APP;Trem2^{ko}), 6–7 month females ($n = 11$ PS2APP;Trem2^{wt} and 13 PS2APP;Trem2^{ko}), 6–7 month males ($n = 16$ PS2APP;Trem2^{wt} and 14 PS2APP;Trem2^{ko}), 12 month females ($n = 15$ PS2APP;Trem2^{wt} and 15 PS2APP;Trem2^{ko}), and 19–22 month males ($n = 12$ PS2APP;Trem2^{wt}, 8 PS2APP;Trem2^{het}, and 7 PS2APP;Trem2^{ko}). Animals were deeply anesthetized with 2.5% tribromoethanol (0.5 ml/25 g body weight) and transcardially perfused with PBS. One brain hemisphere was drop-fixed in 4% PFA for 2 d at 4°C with agitation and then transferred to PBS for histopathological analyses. The other hemisphere was subdivided into cortical and hippocampal tissues that were frozen and stored at -80°C for biochemical assays. Immersion-fixed hemi-brains were cryoprotected, embedded up to 40 per block in a solid matrix, and coronally sectioned at 35 μm (MultiBrain processing by Neuroscience Associates) as previously described (Wang et al., 2011; Kallop et al., 2014). Sheets of sections were stored in cryoprotectant (30% glycerol, 30% ethylene glycol in PBS) at -20°C until use.

Immunohistochemical (IHC) stains for Iba1, CD68, and Gfap were performed at Neuroscience Associates as described previously (Wang et al., 2011), and CD68-stained sections were counterstained with Nissl (0.05% thionine/0.08 M acetate buffer, pH 4.5). Silver stains for amyloid plaque (Campbell-Switzer stain) (Switzer et al., 1993) and neuronal damage/degeneration (amino cupric silver) or “disintegrative degeneration” stain (de Olmos et al., 1994) were also performed at Neuroscience Associates. The bases for these silver stains are given by Switzer (2000) and described at the Neuroscience Associates website (<https://www.neuroscienceassociates.com/technologies/staining/>). IHC and silver stains spanned a broad rostral-caudal range, including 8–11 sections per animal. Stained slides were returned to Genentech for imaging and quantitation, and unused sections were also returned to Genentech for cryoprotected storage until used for additional stains.

For X-34 stains, sheets were mounted onto slides and completely dried. Slides were incubated with 10 μM X-34 in PBS containing 40% ethanol and 0.02 N NaOH for 10 min, followed by 3 quick washes in PBS, differentiation in 80% ethanol for 1 min, and additional 3 quick PBS washes. After applying ProLong Diamond Antifade Mountant (Thermo Fisher Scientific, P36961), slides were covered with no. 1 coverslips. Two sections per animal were stained, with all cohorts stained and analyzed simultaneously.

For costaining of plaque, microglia, and ApoE or dystrophic axons, sheets encompassing 2 or 3 sections per animal containing regions of the rostral and caudal hippocampus were washed in PBS and then PBS plus Triton X-100 (PBST, 0.1%) and then blocked in PBST (0.3%) with 5% BSA and 5% normal donkey serum, then incubated overnight with primary antibodies diluted in PBST (0.3%) plus 1% BSA at 4°C. Microglia were labeled with rabbit anti-Iba1 (Wako, 019-19741, 1:1000) or goat anti-Iba1 (Abcam, ab5076, 1:1000), ApoE with a rabbit monoclonal antibody (Abcam, ab183597, 1:4000), and dystrophic neurites with rat anti-Lamp1 (Abcam, ab25245, 1:2000). Primary antibody incubation was followed by three 10 min washes in PBST, followed by incubation with secondary antibodies for 2 h at room temperature. Donkey anti-rabbit IgG-Alexa555, anti-rat IgG-Alexa647, and anti-goat IgG-Alexa647 (Thermo Fisher Scientific, 1:500) were used as secondary detection reagents. Following the stain, tissue sheets went through three 10 min washes in PBST (0.1%) and three quick washes in PBS. Sheets were mounted onto slides with 0.1% gelatin in PBS and allowed to dry and adhere to the slide at room temperature. To label plaque, slides were then incubated with 10 μM methoxy-X04 in 40% ethanol in PBS for 10 min, washed briefly in PBS, differentiated in 0.2% NaOH in 80% ethanol for 2 min, washed, and then allowed to dry. Slides were coverslipped with added ProLong Gold Antifade Mountant (Thermo Fisher Scientific, P36961). All cohorts were stained and analyzed simultaneously.

Imaging and quantitation of stained sections. Brain tissue samples processed by Neuroscience Associates were imaged on the SCN400 whole-slide scanning system (Leica Microsystems) at 200 \times magnification. MATLAB (The MathWorks) running on a high-performance computing

cluster was used for all whole-slide image analyses performed in a blinded manner. Quantification of CD68 or Iba1 staining and enlarged dark cluster areas was performed using morphometric-based methods as previously described (Le Pichon et al., 2013; Kallop et al., 2014). The large dark “cluster” of CD68 or Iba1⁺ cells coincided with the presence of amyloid plaques. Analysis of amino cupric staining was performed using color thresholds and morphological operations. Plaque area was analyzed from slides stained using the Campbell-Switzer method with plaques appearing with a black or amber hue. Multiple color classifiers spanning narrow ranges in RGB and HSV space were created for positive and negative features. Plaques were segmented using these classifiers and applying adaptive thresholding, Euclidean distance transform, morphological operations, and reconstruction. The percentage plaque load, amino cupric, Iba1, CD68, or Gfap positivity for the entire section were calculated by normalizing the positive pixel area to tissue section area and averaged from 8–11 sections/animal. All images, segmentation overlays, and data were reviewed by a pathologist.

Image acquisition of immunofluorescent slides contained for plaque, microglia, and either ApoE or dystrophic neurites was performed at 200 \times magnification using the Nanoscope S60 or XR (Hamamatsu) digital whole-slide scanner. Ideal exposure for each channel was determined based on samples with the brightest intensity and set for the whole set of slides to run as a batch. Total tissue area was detected by thresholding on the Iba1 signal and merging and processing of the binary masks by morphological operations. Methoxy-X04, Lamp1, ApoE, and Iba1 staining was analyzed using a top-hat filter and local threshold followed by morphological opening and closing. For Lamp1 and methoxy-X04 staining, shape factor, roundness, and solidity features were used to eliminate elongated objects. In addition, a minimum size of 34 μm^2 was applied to exclude small areas of staining. The detected plaques were used as markers in a marker-controlled watershed segmentation to create watershed lines of separation. The plaque mask was then dilated by 17 μm but constrained to be within watershed lines to prevent merging of plaques in close proximity during dilation. Total Lamp1-positive staining was normalized to the whole tissue area. Plaque-associated Lamp1 and Iba1 staining was constrained to be within the mask of dilated area around plaque and was normalized to the same area. Plaque-associated ApoE staining was constrained to be within the mask of plaque + dilated area and normalized to plaque area. Data were averaged from 2 or 3 sections per animal.

For X-34 stains, images were collected with a confocal laser scanning microscope LSM780 (Carl Zeiss) using Zen 2.3 SP1 software (Carl Zeiss). Eleven z-stack images at 1 μm intervals were collected with Plan-Apochromat 20 \times /0.8 M27, and maximum intensity projection images were created using Zen software. Images were collected and processed blind to genotypes. Image analysis was performed using MATLAB in a blinded fashion on the maximum intensity projection of the confocal z-stack. Control images that did not have X-34 positive staining were used to determine an initial threshold to exclude background. A threshold that is >99.99% of all pixel intensities in the control images was applied to all images to determine an initial segmentation mask. The binary masks were then smoothed out using morphological opening and closing. A minimum size of 9 μm^2 was applied to exclude small areas of staining. A threshold corresponding to the 80th and 50th intensity percentile for the pixels within the segmentation mask of all positive images was applied to analyze compact and diffuse area, respectively. Post-threshold morphological operations and size exclusion were performed as described above. The plaque diffuseness index was calculated as follows: $(\text{Area}_{\text{diffuse+compact}} - \text{Area}_{\text{compact}})/\text{Area}_{\text{diffuse+compact}}$. For each animal, data were averaged from two sections per animal, with 3 or 4 images per section consisting of two fields from cortex: one field from dorsal subiculum and/or one field from dentate gyrus molecular layer.

For analysis of methoxy-X04 or ApoE colocalization within Iba1⁺ microglia, images were collected from the contained slides described above for the 12 month female cohort of animals using confocal laser scanning microscope LSM780 (Carl Zeiss) with Zen 2.3 SP1 software (Carl Zeiss). Eleven z-stack images at 1 μm intervals were collected from the cortex with Plan-Apochromat 20 \times /0.8 M27. To determine colocalization of ApoE and Iba1 staining, or methoxy-X04 and Iba1 staining, we

calculated the Mander's colocalization coefficients using the ImageJ plugin JACoP, as described previously (Dunn et al., 2011). The same thresholds were consistently used to identify the Iba1, ApoE, or methoxy-X04 channel across animal samples. Calculations were performed on the entire z-stack of images.

A β peptide measurements. Frozen hippocampal tissues, described above, were homogenized in 10 volumes of TBS (50 mM Tris pH 7.5, 150 mM NaCl) including complete EDTA-free protease inhibitor mixture (Roche Diagnostics) with aprotinin (20 $\mu\text{g}/\text{ml}$) and leupeptin (10 $\mu\text{g}/\text{ml}$) in a QIAGEN TissueLyser II (3 min at 30 Hz). Samples were then centrifuged at 20,000 $\times g$ for 20 min at 4°C. Supernatants were collected as the “TBS fraction” and stored at -80°C until analyzed. The pellet was then homogenized in 10 volumes of 5 M guanidine HCl using the TissueLyser II and then placed on a rotisserie for 3 h at room temperature. Samples were diluted 1:10 in a casein buffer (0.25% casein/5 mM EDTA, pH 8.0, in PBS), including aprotinin (20 $\mu\text{g}/\text{ml}$) and leupeptin (10 $\mu\text{g}/\text{ml}$), vortexed and centrifuged at 20,000 $\times g$ for 20 min at 4°C. Supernatants were collected as “GuHCl fractions.” A β 40 and A β 42 concentrations in mouse hippocampal samples were measured using an ELISA. Briefly, rabbit polyclonal antibody specific for the C terminus of A β 40 or A β 42 (Millipore) was coated onto plates, and biotinylated monoclonal anti-A β 1-16 (Covance, clone 6E10) was used for detection.

For dot blot analyses, $\sim 10 \mu\text{g}$ in 1 μl of lysate (TBS soluble fraction of homogenized mouse hippocampus) was blotted onto nitrocellulose membranes (#LC2001, Invitrogen) and incubated for at least 1 h at room temperature to ensure that the blots were dry. The membrane was blocked with Blocking Buffer (MB-070, Rockland Immunochemicals) with added 0.01% Tween 20, for 1 h at room temperature. The membrane was incubated with Amyloid Fibrils OC (Sigma Millipore, AB2286), Oligomer A11 (Thermo Fisher Scientific, AHB0052), 4G8 (BioLegend, 800703), or 6E10 (BioLegend, 803015) primary antibody diluted 1:1000 in Blocking Buffer for 1 h at room temperature. Total protein was normalized with mouse anti- β -actin (Cell Signaling Technology, 8H10D10, 1:10,000) or rabbit anti-GAPDH (Novus Biological, NB300-323, 1:10,000). After primary antibody incubation, membranes were washed 3 times (10 min each) with TBST (50 mM Tris, 0.5 M NaCl, 0.01% Tween 20). The membrane was incubated with secondary antibodies in Blocking Buffer at 1:15,000 dilution (IRDye 800CW donkey anti-rabbit IgG and IRDye 680LT donkey anti-mouse IgG, LI-COR Biosciences, 926-32213, 926-32212, 926-68022, and 926-68023) for 1 h at room temperature. Membrane was washed 3 times (10 min each) in TBST on rocker. Blots were scanned on Odyssey/LICOR scanner for signals followed by image analysis in Image Studio (version 5.2.5, LI-COR Biosciences).

CSF collection and neurofilament light chain (NfL) analysis. A separate, mixed sex cohort of 12 month PS2APP;Trem2^{wt} ($n = 8$) and PS2APP;Trem2^{ko} mice ($n = 8$) was anesthetized, and CSF was collected from the cisterna magna and placed on ice; then blood was collected from terminal cardiac puncture, placed into EDTA collection tubes, and centrifuged at 20,000 $\times g$ for 2 min. (The two genotype groups in this analysis were not littermates since we had not collected plasma or CSF from our original cohorts, and we assembled this cohort just for NfL measurements due to a recommendation received during peer review.) Plasma was collected into tubes and stored at -80°C until transfer. CSF samples were diluted 1:10 in 0.1% BSA in TBS and then stored at -80°C until transfer. Plasma and CSF samples were sent to Quanterix for NfL measurements using the Simoa NF-Light Advantage Kit (product 103186). The Simoa assay is a 2 step digital immunoassay, which measures the quantity of NfL in samples using the Simoa HD-1 Analyzer and Single Molecule Array (Simoa) technology.

Two-photon imaging of plaque and dendritic spine measurements. The somatosensory cortex from PS2APP mice carrying the Thy1:GFP-M transgene and different Trem2 genotypes was imaged *ex vivo* via 2-photon microscopy. Single-sex cohorts used for this purpose included 6 month PS2APP females ($n = 7$ for per Trem2 genotype, used for both plaque counts and dendritic spine measurements) and 8 month PS2APP males ($n = 6$ per Trem2 genotype, used only for plaque counts). At 24 h before brain collection, animals received intraperitoneal injections of methoxy-X04 (10 mg/kg) to label amyloid structures (Klunk et al., 2002).

Animals were anesthetized using isoflurane and transcardially perfused with 10 ml PBS followed by 10 ml of 4% PFA + 10% sucrose in PBS, and the collected brains were fixed overnight in 4% PFA + 10% sucrose in PBS at 4°C. After fixation, brains were mounted in agarose and immersed in PBS. Imaging and analysis were performed under blinded conditions.

Apical dendrites and their spines in somatosensory cortex upper layers were imaged *en bloc* via a two-photon laser-scanning microscope (Ultima In Vivo Multiphoton Microscopy System, Prairie Technologies) using a Ti:sapphire laser (MaiTai DeepSee Spectra Physics, Newport) tuned to 840 nm and a 60 \times numerical aperture 1.0 immersion objective lens (Olympus) with pixel resolution of 0.1 μ m/pixel across a 1024 \times 1024 pixel FOV using 1.0 μ m steps, with stack depth determined by the slant of the dendritic branch being imaged. For comparison of spine density relative to plaques in PS2APP animals, an FOV containing a dendrite and nearby plaque within 20 μ m was considered “near plaque” and an FOV containing only a dendrite with no visible plaque was considered “away from plaque.” To meet the “away from plaque” criteria, we confirmed that no plaque was present in the FOV and at least 100 μ m outside of the containing FOV. From each brain, at least five dendrites per condition (near plaque, away from plaque) were imaged. Dendritic spine density and size measurements were generated using custom, semi-automated image analysis routines in MATLAB (The MathWorks). Spine density was estimated as the total number of visible dendritic spines divided by the corresponding length of dendrite. Relative spine volumes were estimated for each detected spine based on the number of corresponding GFP⁺ pixels in *x*, *y*, *z* dimensions above a local threshold applied as part of an automated image segmentation algorithm. For *en bloc* plaque measurements, larger-volume stacks were collected using a 20 \times immersion objective lens across a 1024 \times 1024 pixel FOV with 2 μ m steps (~200 μ m depth). Plaque density was quantified by a threshold-based MATLAB routine designed to automatically identify methoxy-X04-labeled plaques.

Statistical analysis. All values are expressed as mean \pm SEM. Statistical analysis was performed using the JMP (version 14.2, SAS Institute) or Prism (version 8.3.0 for Mac, GraphPad) software packages. To compare differences between PS2APP;Trem2^{wt} and PS2APP;Trem2^{ko} groups, we performed unpaired *t* tests. For comparisons of three or more groups, we performed one-way ANOVA followed by Tukey’s multiple-comparisons test. The 6–7 month cohort of male and female mice was purposely analyzed separately to determine the effects of *Trem2* deficiency in each sex since female mice have accelerated amyloid pathology compared with males, and we did not want an analysis of interactions between sex and *Trem2* genotype to be confounded by the age-dependent differences in pathology between males and females.

Results

Plaque-associated microgliosis is impaired in PS2APP;Trem2^{ko} microglia

PS2APP mice express transgenes encoding familial AD mutations in human presenilin 2 (PS2 N141I) and APP (APP K670N/M671L). By 4 months of age, the first deposits of β -amyloid plaque are detected, with age-dependent plaque accumulation occurring faster in females than in males (Ozmen et al., 2009; Kallop et al., 2014). To determine the role of *Trem2* in the progression of amyloid disease pathology, we crossed PS2APP mice with *Trem2*-deficient mice and examined plaque-related phenotypes in single-sex groups at various stages of pathology. We found a stark reduction in Iba1⁺ microglial clusters in PS2APP;Trem2^{ko} mice at 4, 6–7, 12, and 19–22 months compared with PS2APP;Trem2^{wt} (Fig. 1*A,B*). In addition, PS2APP;Trem2^{ko} brains showed reduced staining for CD68 marking active microglial lysosomes by IHC (Fig. 1*C,D*), reduced percentage of CD45^{high} (“activated”) microglia by flow cytometry (Fig. 1*E,F*), and reduced percentage of methoxy-X04⁺ (amyloid-containing) microglia by flow cytometry (Fig. 1*G,H*). Analysis of confocal *z*-stack images of cortical tissue from 12 month PS2APP;Trem2^{ko} animals also found a significant reduction in the fraction of Iba1

and methoxy-X04 signals that colocalized with each other (Fig. 1-1, available at <https://doi.org/10.1523/JNEUROSCI.1871-19.2019.f1-1>). We also observed reductions in total Iba1 and Gfap staining at the later ages, indicative of reduced extents of microgliosis and astrogliosis, respectively, in PS2APP;Trem2^{ko} mice (Fig. 1-1, available at <https://doi.org/10.1523/JNEUROSCI.1871-19.2019.f1-1>). These observations were consistent with reports of *Trem2* deletion in other β -amyloidosis models (Jay et al., 2015; Wang et al., 2015, 2016; Yuan et al., 2016; Parhizkar et al., 2019) and suggested that *Trem2* deficiency impairs the ability of microglia to engage plaques and phagocytose A β fibrils/aggregates.

Trem2-dependent induction of the proliferation and neurodegeneration-related gene expression modules

To further characterize the attenuated microglial response to β -amyloid pathology in PS2APP;Trem2^{ko} mice, we FACS-isolated the resident myeloid cell population from the cortex+hippocampus of 14–15 month PS2APP;Trem2^{wt} versus PS2APP;Trem2^{ko} mice and compared their transcriptomic profiles by RNA sequencing (raw RNA-Seq data deposited in NCBI GEO under accession number GSE140744). Although not affording single-cell resolution, our approach provided certain overall advantages (genome-wide analysis, robust detection of low-copy transcripts, and avoidance of artifactual gene expression that occurs during warm-temperature dissociations) compared with other approaches for transcription profiling of Trem2^{ko} microglia in β -amyloid models that used different cell isolation techniques and/or different RNA detection methods, such as microarray, Nanostring, or single-cell RNAseq (Wang et al., 2015; Keren-Shaul et al., 2017; Krasemann et al., 2017; Griuciu et al., 2019).

Applying cutoffs of ≥ 2 -fold change and adjusted *p* value ≤ 0.05 , we observed only 7 transcripts with increased abundance in PS2APP;Trem2^{ko} versus PS2APP;Trem2^{wt} microglia (excluding *Trem11*, an artifact of the KO cassette insertion) (Kang et al., 2018). In contrast, 144 transcripts (excluding *Trem2*) showed reduced abundance in PS2APP;Trem2^{ko} compared with PS2APP;Trem2^{wt} microglia using the same cutoffs (Fig. 2*A*; for extended data table of genome-wide expression values for each sample and summary statistics for differential gene expression, see Fig. 2-1, available at <https://doi.org/10.1523/JNEUROSCI.1871-19.2019.f2-1>). The majority of these transcripts showed upregulation in microglial expression profiles from the PS2APP model (Friedman et al., 2018) and other models of β -amyloid pathology (Orre et al., 2014; Wang et al., 2015) compared with nontransgenic mice (Fig. 2*A*). Therefore, their reduced expression in PS2APP;Trem2^{ko} microglia is another manifestation of the impaired microglial response to β -amyloid pathology. The dependence of these transcripts on *Trem2* for their induction in PS2APP microglia was approximately concordant with published data from sorted microglial populations from the 5x*FAD* model (Wang et al., 2015) (Fig. 2*A*).

Four of the eight most starkly reduced transcripts (in terms of fold change) in PS2APP;Trem2^{ko} microglia are regulators of canonical Wnt signaling or proliferation (*Dkk2*, *Wif1*, *Ctnna3*, and *Asb11*) (Fig. 2*B*). *Dkk2*, *Wif1*, and *Ctnna3* can all negatively regulate Wnt activity (Hsieh et al., 1999; Busby et al., 2004; Gage et al., 2008), whereas *Asb11* is important for maintaining progenitor cell activity in multiple cell types (Diks et al., 2006; Tee et al., 2012). Although the lack of induction for negative Wnt regulators might suggest that Wnt-related signaling was enhanced in Trem2^{ko} microglia, another possibility is that Wnt-related signaling was impaired since *Dkk2* is also a context-dependent ac-

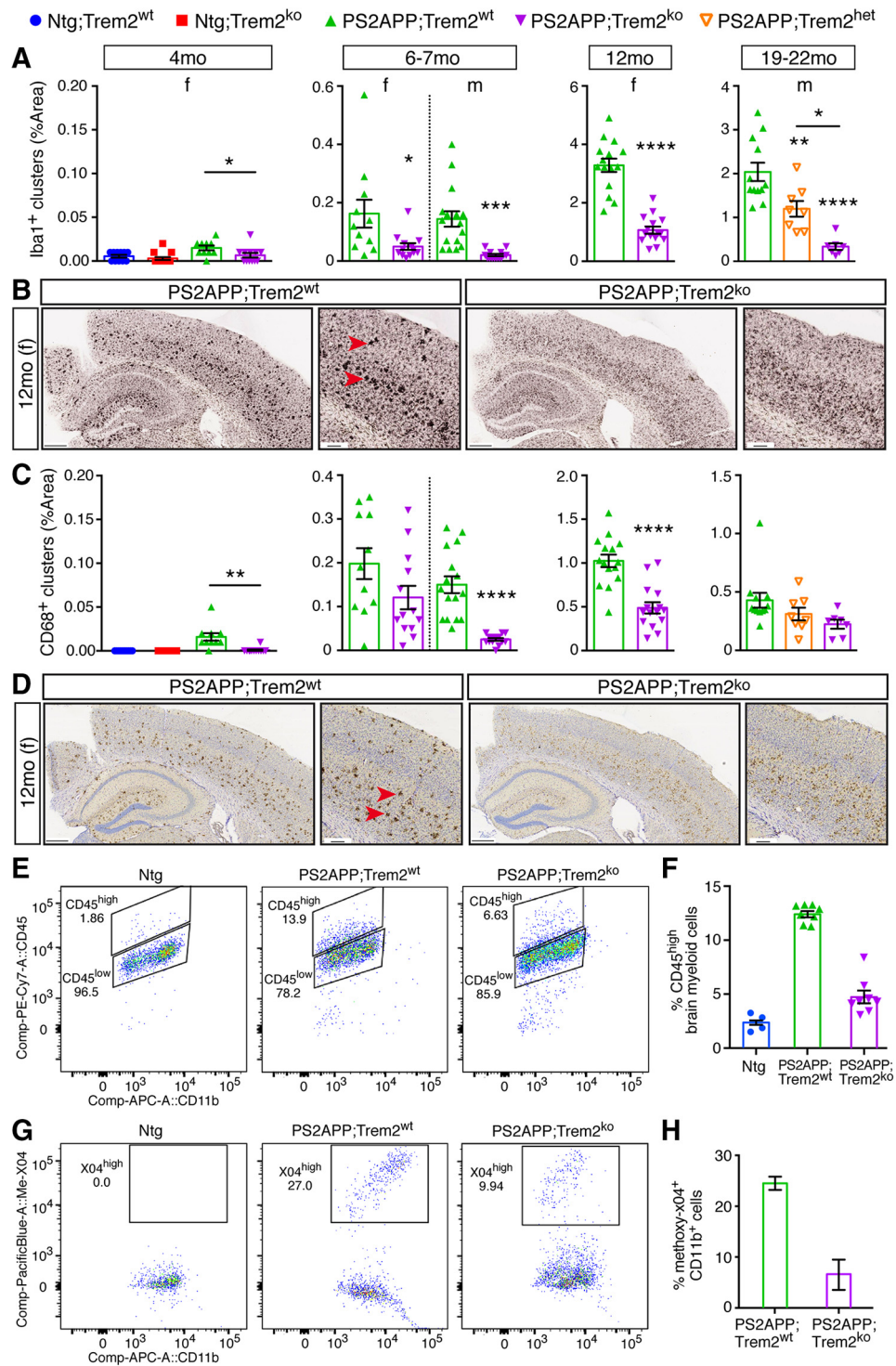


Figure 1. Trem2 deletion impairs microglial clustering, activation, and plaque uptake in PS2APP β -amyloidosis model. **A**, Immunohistochemical detection of microglial clustering in transgenic PS2APP mice or nontransgenic (Ntg) controls with WT (wt), heterozygous (het), or homozygous KO (ko) Trem2 alleles. For analysis of total, rather than clustered, Iba1 signal, see Figure 1-1 (available at <https://doi.org/10.1523/JNEUROSCI.1871-19.2019.f1-1>). Quantification of the percent area covered by clusters of Iba1⁺ microglia was measured from coronal sections of female mice at 4, 6–7, and 12 months of age, and from male mice at 6–7 and 19–22 months of age. Each data point represents the composite (average) histological score from several sections of an individual mouse. Bars and lines represent mean \pm SEM. Unpaired *t* test for most cohorts, or by ANOVA followed by Tukey’s multiple-comparison test for the 19–22 month cohort with three genotypes: **p* < 0.05, ***p* < 0.01, ****p* < 0.001, *****p* < 0.0001 versus PS2APP;Trem2^{wt} or as indicated. **B**, Representative low (left, scale bar, 400 μ m) and high (right, scale bar, 100 μ m) magnification images of Iba1⁺ staining in 12 month female mice are shown. Iba1⁺ clusters (red arrowheads) showed reduced presence across Trem2^{ko} mice at all ages. **C, D**, Same as in **A** and **B**, except analyzing active microglial lysosomes as indicated by CD68 protein expression. **E**, Representative flow cytometry plots measuring CD45 immunoreactivity (low or high) of CD11b⁺ brain-resident myeloid cells from 14 month PS2APP mice with or without Trem2 and from Ntg mice. **F**, Percent of brain-resident myeloid cells with high CD45 expression measured from several mice of each genotype. Bars and lines represent mean \pm SEM. **G, H**, Same as in **E** and **F**, except analyzing plaque content in brain CD11b⁺ cells from ~12 months mice injected with methoxy-X04 dye to stain amyloid material. Ntg mice are not plotted in **H** since they have zero methoxy labeling. *n* = 3 in Trem2^{wt}; *n* = 2 in Trem2^{ko}. For histological analysis of methoxy-X04 and Iba1⁺ microglia colocalization in sections, see Figure 1-1 (available at <https://doi.org/10.1523/JNEUROSCI.1871-19.2019.f1-1>).

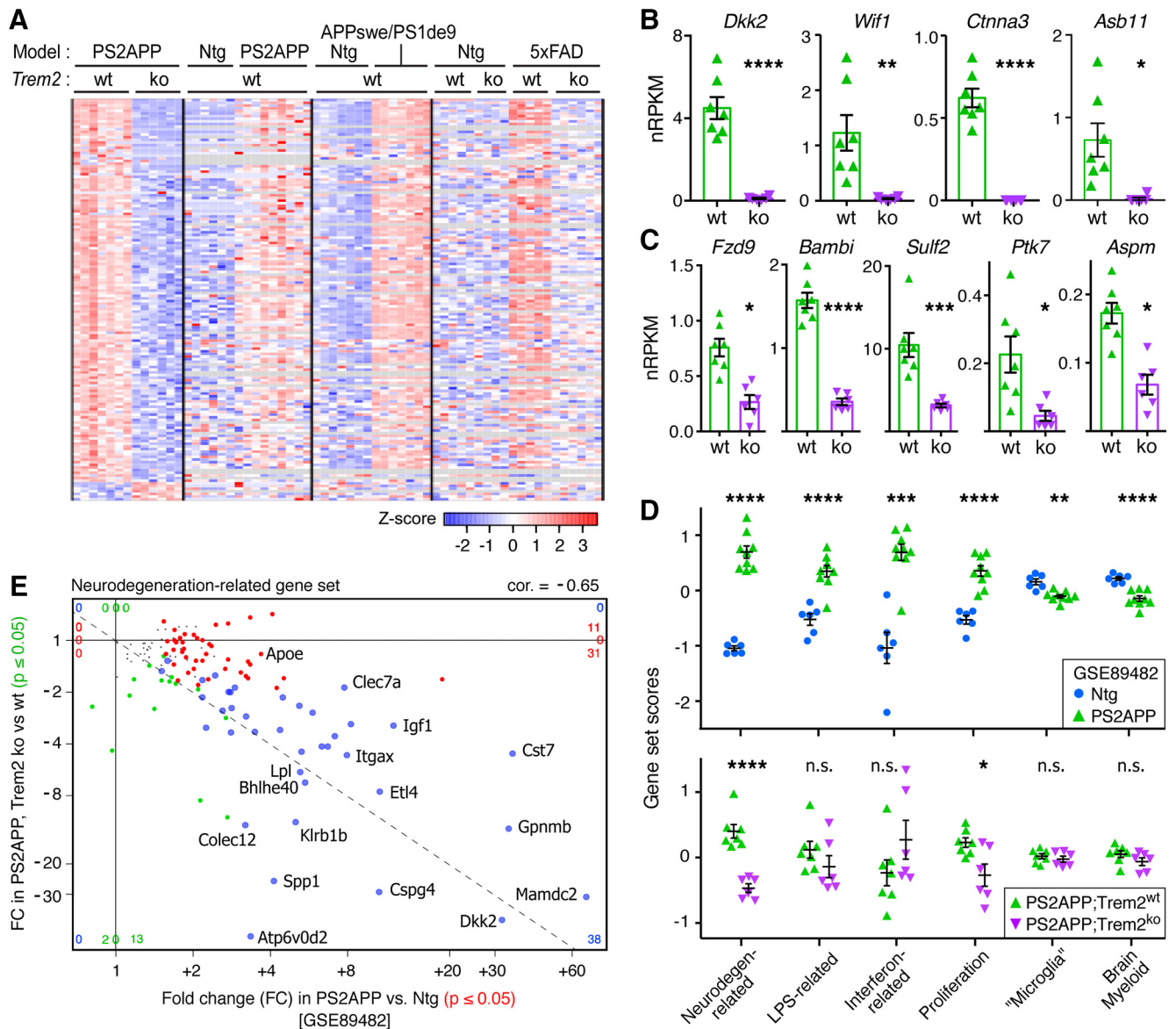


Figure 2. Induction of Neurodegeneration-related and Proliferation gene modules and Wnt-related signaling components is impaired in Trem2^{ko} microglia. **A**, Heat map of differentially expressed genes (DEGs) between Trem2^{wt} and Trem2^{ko} microglia from 14 month PS2APP mouse brains (fold change ≥ 2 , adjusted $p \leq 0.05$), cross-referenced against previously published datasets from the PS2APP (GSE89482), APPswe/PS1de9 (GSE74615), and 5xFAD (GSE65067) models. Each row is a DEG, and each column is a microglial sort from a different mouse. z-score coloring represents a sample's distance in SDs from the mean expression value for a given gene across samples within a dataset. Most of the downregulated DEGs in Trem2^{ko} microglia were typically induced in models of β -amyloid pathology, and the majority also showed impaired microglial induction in Trem2^{ko} 5xFAD mice. For a complete list of genome-wide expression values in PS2APP;Trem2^{wt} and PS2APP;Trem2^{ko} microglia, see Figure 2-1 (available at <https://doi.org/10.1523/JNEUROSCI.1871-19.2019.f2-1>). **B**, Induction of the Wnt/proliferation regulators *Dkk2*, *Wif1*, *Ctnna3*, and *Asb11* was completely impaired in Trem2^{ko} microglia of PS2APP mice. **C**, DEGs identified by GO analysis as “positive regulators of Wnt signaling” with reduced expression in PS2APP;Trem2^{ko} microglia included *Fzd9*, *Sulf2*, *Bambi*, *Ptk7*, *Aspm*, and *Dkk2*. **B**, **C**, Bars and lines represent mean \pm SEM, with each data point representing microglial gene expression level from a given mouse. For genes in **B** and **C**, see also Figure 2-2 (available at <https://doi.org/10.1523/JNEUROSCI.1871-19.2019.f2-2>), showing microglial expression in the 5xFAD model with or without Trem2 (data from independent investigators). **D**, Top, Analysis of previously published expression profiles from the PS2APP model (GSE89482) indicated that six gene expression modules for brain myeloid cells (defined by Friedman et al., 2018) showed altered expression in microglia from brains with β -amyloid pathology. Bottom, Analysis of Trem2^{ko} and Trem2^{wt} microglia expression profiles from PS2APP mice showed that the Neurodegeneration-related and Proliferation gene sets showed significant Trem2 dependence. For data from independent investigators showing enriched expression of Proliferation module in 5xFAD model microglia and its dependence on Trem2 for full induction, see also Figure 2-2 (available at <https://doi.org/10.1523/JNEUROSCI.1871-19.2019.f2-2>). For heat map displays of all individual genes in each module, see also Figure 2-3 (available at <https://doi.org/10.1523/JNEUROSCI.1871-19.2019.f2-3>). Each data point represents a gene set expression score for microglia isolated from a given mouse. Lines indicate mean \pm SEM. Two-tailed *t* tests assuming unequal variance between groups: * $p < 0.05$, ** $p < 0.01$, *** $p < 0.001$, **** $p < 0.0001$. **E**, Four-way plot of Neurodegeneration-related gene set, with each point representing a gene's fold change in expression between PS2APP versus nontransgenic microglia on the x axis (red and blue points, adjusted $p < 0.05$) and between PS2APP;Trem2^{ko} versus PS2APP;Trem2^{wt} microglia on the y axis (green and blue points, adjusted $p < 0.05$). Blue points represent significant differential expression in both datasets. Tiny black points represent genes not differentially expressed in either dataset.

tivator of the pathway (Wu et al., 2000; Mao and Niehrs, 2003; Devotta et al., 2018) and since induction of regulators, including *Wif1*, can occur downstream of active β -catenin as negative feedback (Diep et al., 2004; Boerboom et al., 2006). Supporting this

interpretation, the GO knowledge base identified “positive regulation of canonical Wnt signaling pathway” as a biological process overrepresented (fold enrichment = 10.3, FDR = 0.026) among the 144 transcripts with ≥ 2 -fold reduced abundance in

PS2APP;Trem2^{ko} microglia (Fig. 2-2A, available at <https://doi.org/10.1523/JNEUROSCI.1871-19.2019.f2-2>), with six positive factors in Wnt signaling showing reduced expression including *Fzd9* (Karasawa et al., 2002), *Sulf2* (Lai et al., 2010), *Bambi* (Lin et al., 2008), *Ptk7* (Berger et al., 2017), and *Aspm* (Buchman et al., 2011) along with *Dkk2* (Fig. 2C). We also analyzed recently published microglia RNA-Seq expression profiles from the 5xFAD model (Griciuc et al., 2019) and observed similar Trem2-dependent induction for the nine above-mentioned genes, with the exception of *Ptk7* (Fig. 2-2B, available at <https://doi.org/10.1523/JNEUROSCI.1871-19.2019.f2-2>). The reduced expression of Wnt-related signaling components and regulators in PS2APP;Trem2^{ko} microglia may be consistent with previous reports of coordinated signaling between Trem2 and β -catenin pathways within microglia (Zheng et al., 2017; Zulfiqar and Tanriöver, 2017).

Other GO biological processes implicated as being downregulated in PS2APP;Trem2^{ko} microglia included positive regulation of bone resorption (fold enrichment = 24.6, FDR = 0.030), protein kinase B signaling (fold enrichment = 16.2, FDR = 0.047), negative regulation of tumor necrosis factor production (fold enrichment = 14.1, FDR = 0.026), positive regulation of smooth muscle cell migration (fold enrichment = 13.9, FDR = 0.025), transmembrane receptor protein tyrosine kinase signaling pathway (fold enrichment = 5.9, FDR = 0.0037), and actin cytoskeleton reorganization (fold enrichment = 3.9, FDR = 0.044) (Fig. 2-2A, available at <https://doi.org/10.1523/JNEUROSCI.1871-19.2019.f2-2>). The Trem2-dependent genes identified in these processes may underlie described roles for Trem2 in osteoclast function (Cella et al., 2003; Paloneva et al., 2003), AKT and mTOR signaling (Ulland et al., 2017), attenuation of proinflammatory macrophage activation (Turnbull et al., 2006), chemotaxis (Mazaheri et al., 2017), and DAP12 signaling (Bouchon et al., 2001).

We recently defined a number of gene expression modules that can be used to characterize the diverse ways that microglia respond to environmental and genetic perturbations (Friedman et al., 2018). In PS2APP compared with nontransgenic microglia, several of these gene sets were upregulated, including the Neurodegeneration-related, Interferon-related, Proliferation, and LPS-related modules, whereas the Microglia and Brain Myeloid modules that typify microglia in their “homeostatic” or “resting” state were modestly but significantly downregulated (Fig. 2D; Fig. 2-3, available at <https://doi.org/10.1523/JNEUROSCI.1871-19.2019.f2-3>). The entirety of these changes is approximately equivalent to the so-called DAM (Keren-Shaul et al., 2017) or MgND (Krasemann et al., 2017) microglial activation profiles. These findings underscore the utility of these gene modules in characterizing microglial activation states. For instance, even though only 5 of 82 genes in the Proliferation module were upregulated strongly enough in PS2APP microglia to reach genome-wide significance (adjusted $p \leq 0.05$), the overall expression of the module was clearly enriched compared with microglia from nontransgenic mice (Fig. 2D; Fig. 2-3, available at <https://doi.org/10.1523/JNEUROSCI.1871-19.2019.f2-3>).

We next analyzed the degree to which these modular changes in microglial gene expression in PS2APP mice depended on Trem2. Again, despite only 2 of 82 genes (*Ccna2* and *Aspm*) showing significant reduction in transcript abundance after correction for genome-wide analysis, the overall induction of the Proliferation module was compromised in PS2APP;Trem2^{ko} microglia (Fig. 2D; Fig. 2-3, available at <https://doi.org/10.1523/JNEUROSCI.1871-19.2019.f2-3>). We also observed less induc-

tion of the Proliferation module in Trem2^{ko} microglia expression profiles from the 5xFAD model (Griciuc et al., 2019) (Fig. 2-2C, available at <https://doi.org/10.1523/JNEUROSCI.1871-19.2019.f2-2>). The reduced expression of proliferation-related genes was consistent with the notion mentioned above that Wnt-related signaling was impaired and also corroborated reports from other β -amyloid models that proliferation markers, such as Ki67 or BrdU, were observed less frequently in Trem2-deficient microglia (Wang et al., 2016; Jay et al., 2017a).

As expected, the Neurodegeneration-related gene set, which overlaps with the so-called DAM (Keren-Shaul et al., 2017) and MgND (Krasemann et al., 2017) genes but relates more specifically to neurodegenerative disease models, was notably impaired in PS2APP;Trem2^{ko} microglia (Fig. 2D; Fig. 2-3, available at <https://doi.org/10.1523/JNEUROSCI.1871-19.2019.f2-3>). Of the 134 genes in this set, 80 showed upregulation in PS2APP versus normal microglia (Friedman et al., 2018), and approximately half of these showed impaired induction in PS2APP;Trem2^{ko} microglia (adjusted p values ≤ 0.05) (Fig. 2E). Unlike the clear requirement of Trem2 for induction of many genes in the Neurodegeneration-related gene set, the downregulation of the Microglia and Brain Myeloid modules that normally occurs during any CNS challenge (Friedman et al., 2018) was not prevented by Trem2 deletion since expression of these modules was similar in PS2APP;Trem2^{wt} and PS2APP;Trem2^{ko} microglia (Fig. 2D; Fig. 2-3, available at <https://doi.org/10.1523/JNEUROSCI.1871-19.2019.f2-3>). No effect of Trem2 deletion on the induction of the LPS-related and Interferon-related modules was observed. Overall, our results are similar to previous analysis of the 5xFAD model, in which the microglial induction of many DAM genes showed substantial Trem2 dependence whereas the downregulation of so-called microglial “homeostatic” genes appeared largely Trem2-independent (Keren-Shaul et al., 2017).

Plaque load is reduced in aged PS2APP;Trem2^{ko} mice

In the 5xFAD mouse model, plaque load was reportedly unchanged in 4 month Trem2^{ko} mice but increased in 8 month Trem2^{ko} hippocampus (Wang et al., 2015, 2016; Yuan et al., 2016). In the APPPS1 model, plaque load was reduced in Trem2^{ko} brains at 2 months, reduced or unchanged at 4 months, and increased in the cortex at 8 months (Jay et al., 2015, 2017a).

The reductions in microglial clustering and amyloid engulfment in PS2APP;Trem2^{ko} mice (Fig. 1) suggested that more plaque might accumulate over time in these brains, relative to PS2APP;Trem2^{wt} mice. Indeed, using the Campbell-Switzer silver stain to label amyloid plaque (Campbell et al., 1987; Switzer, 2000), we observed that plaque burden was increased in 6–7 month PS2APP;Trem2^{ko} females, and trending upward but not reaching significance in 6–7 month PS2APP;Trem2^{ko} males (Fig. 3A,B). We observed similar results in distinct cohorts of 6 month females and 8 month males by *in vivo* labeling of plaque using methoxy-X04 injection, followed by fixation and two-photon imaging of intact somatosensory cortex (Fig. 3-1, available at <https://doi.org/10.1523/JNEUROSCI.1871-19.2019.f3-1>). We did not observe any effect of Trem2 deletion on the low levels of plaque deposition detected at the earliest stage examined (4 months).

We expected to see further exacerbation of amyloid plaque load in Trem2-deficient brains at more advanced ages, but, to our surprise, plaque load was reduced in 12 month PS2APP;Trem2^{ko} females and in 19–22 month PS2APP;Trem2^{ko} males compared with PS2APP;Trem2^{wt} mice (Fig. 3A,B). An intermediate reduction in plaque load was observed in Trem2 heterozygous

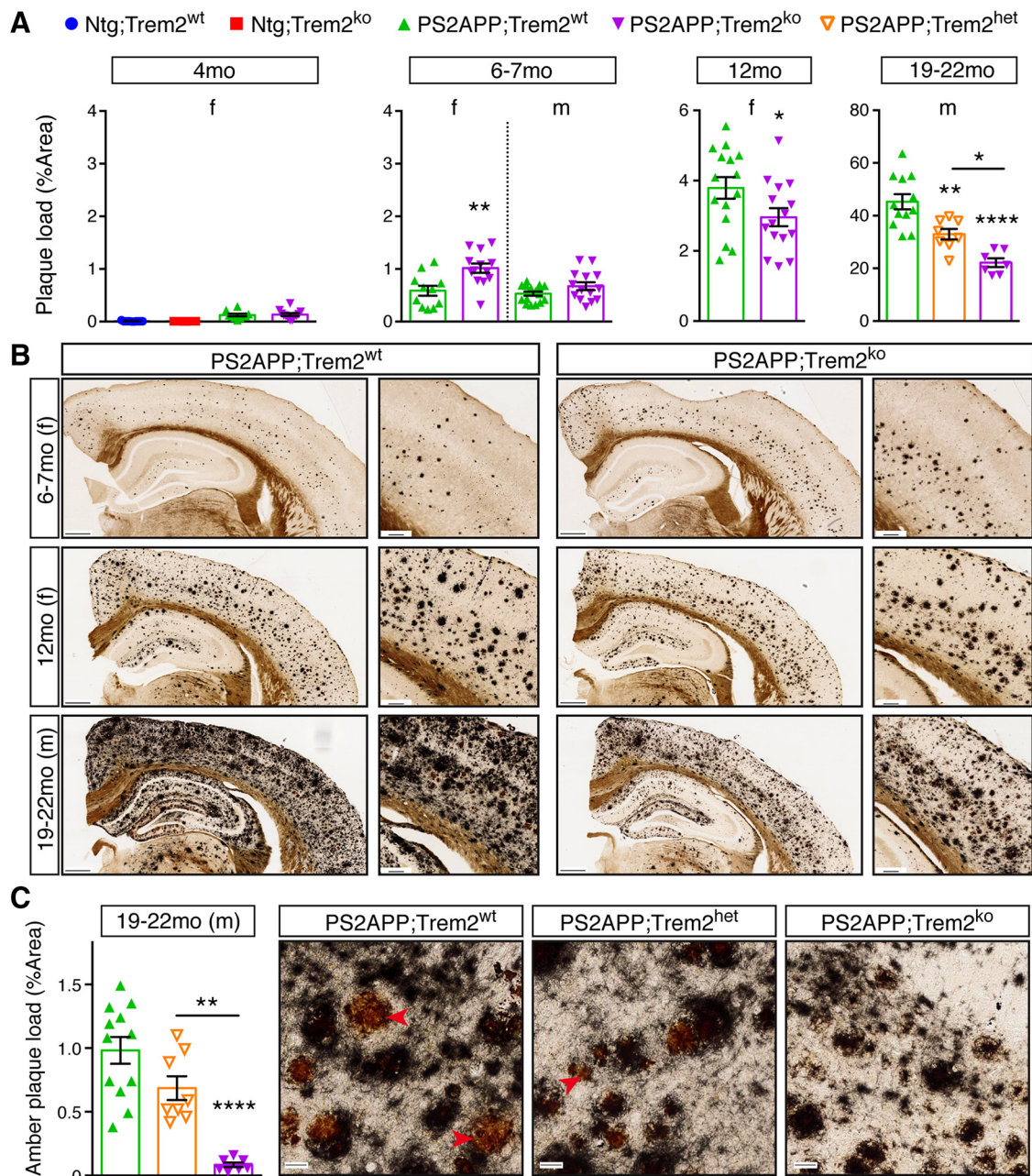


Figure 3. Trem2 deletion shows age- and sex-dependent effects on amyloid plaque pathology, with reduced plaque accumulation at later ages. **A, B,** Amyloid plaque was visualized using the Campbell-Switzer silver stain method in nontransgenic (Ntg) controls or transgenic PS2APP mice with WT (wt), heterozygous (het), or homozygous KO (ko) Trem2 alleles. Quantification of the percent area covered by amyloid plaque was measured from coronal sections of indicated sex and age. Representative low (left, scale bar, 400 μm) and high (right, scale bar, 100 μm) magnification images of amyloid stains are shown. In the absence of Trem2, plaque loads were elevated in 6–7 month females but reduced in 12 month females and in 19–22 month males. For two-photon imaging of methoxy-X04-labeled plaque in somatosensory cortex of 6 month females and 8 month males, see also Figure 3-1 (available at <https://doi.org/10.1523/JNEUROSCI.1871-19.2019.f3-1>). **C,** The Campbell-Switzer silver stain turns highly mature plaque cores amber (red arrowheads). Quantification plot (left) and representative images (right, scale bar, 20 μm) of amber core frequency in 19–22 month male mice. Error bars indicate mean ± SEM. Unpaired *t* test or ANOVA followed by Tukey’s multiple-comparison test: **p* < 0.05, ***p* < 0.01, *****p* < 0.0001 versus PS2APP;Trem2^{wt} or as indicated.

(PS2APP;Trem2^{het}) mice at 19–22 months (the only age where heterozygous mice were analyzed) (Fig. 3A). At this age, the Campbell-Switzer stain also revealed a distinctive pattern of “amber core” amyloid staining in PS2APP brains (Fig. 3C), thought to represent a mature form of highly condensed plaque. These amber cores were reduced in PS2APP;Trem2^{het} and nearly absent in PS2APP;Trem2^{ko} brains, indicating that Trem2-dependent microglial activity is essential for the formation of these particular amyloid structures.

Overall, our results are reminiscent of a recent study of APPPS1 mice, which showed that Trem2 deletion produced increased seeding of amyloid plaques at early ages but slower rates of amyloid plaque accumulation at later ages (Parhizkar et al., 2019).

Reduced plaque consolidation, elevated neurotoxic Aβ species, and ApoE-laden microglia in Trem2-deficient brains
 In contrast to the effects of Trem2 deletion on total plaque burden that varied with age or sex, we observed consistent changes in

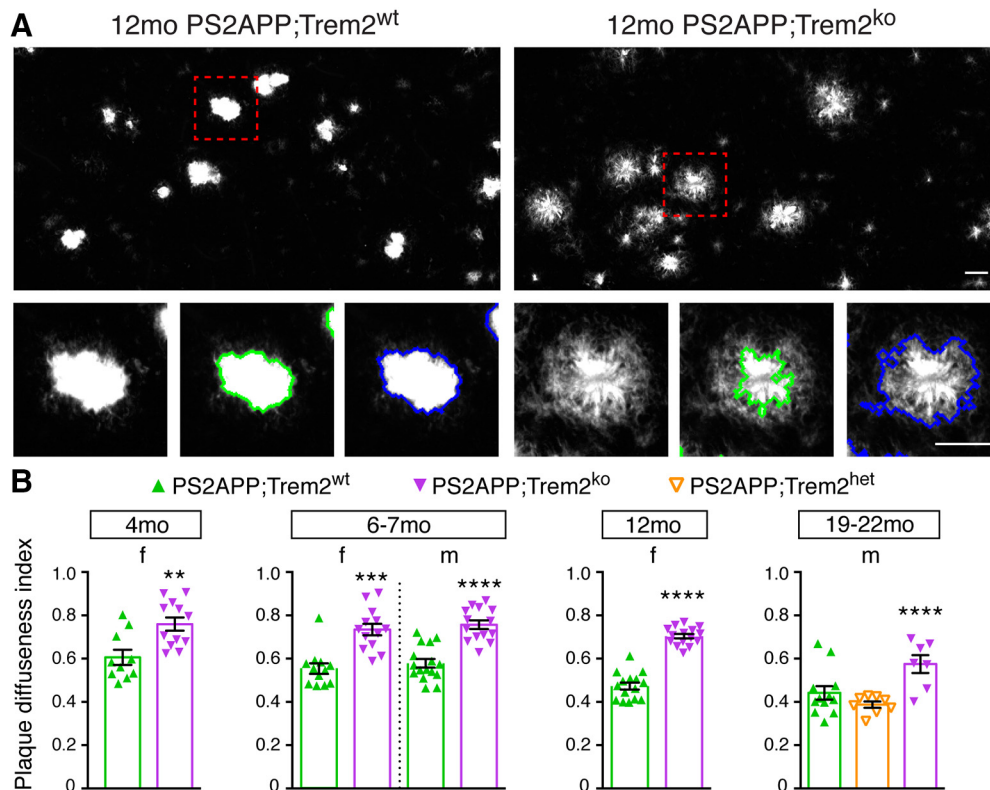


Figure 4. *Trem2* deletion impairs the consolidation of β -amyloid into dense plaque. **A**, β -amyloid plaques were visualized by X-34 staining and confocal z-stack imaging. Representative maximum projection images of X-34⁺ plaques from 12 month PS2APP females of different *Trem2* genotypes are shown (top). High-magnification images show a representative plaque from each genotype with the outlined masks used to delineate the compact core (green) and compact + diffuse (blue) areas of the plaque (bottom). Scale bars, 20 μ m. **B**, The diffuseness index (see Materials and Methods) of the X-34⁺ plaques in cohorts of the indicated age and sex was quantified. Each data point represents 1 animal's plaque diffuseness index averaged from 3 to 4 FOV. Error bars indicate mean \pm SEM. Unpaired *t* test or ANOVA followed by Tukey's multiple-comparison test: ***p* < 0.01, ****p* < 0.001, *****p* < 0.0001 versus PS2APP;Trem2^{wt}.

plaque compaction and composition across ages and sexes. We used the X-34 stain and confocal microscopy to visualize plaque morphology. Although we were blinded to *Trem2* genotype, there was an obvious difference in plaque appearance between PS2APP;Trem2^{wt} and PS2APP;Trem2^{ko} brains, with X-34⁺ structures in PS2APP;Trem2^{ko} brains looking more splayed and less compact (Fig. 4A), similar to descriptions of Trem2-dependent plaque alterations in other β -amyloid models (Wang et al., 2016; Yuan et al., 2016). Using an algorithm based on X-34 signal intensity to quantify the degree of plaque diffuseness, we observed that plaque morphologies were significantly more diffuse in PS2APP;Trem2^{ko} brains in both sexes at all ages tested (Fig. 4B).

Because stains, such as Campbell-Switzer, methoxy-X04, and X-34, only label fibrillar amyloid structures, we also measured the total abundance of A β 40 and A β 42 peptides in soluble (TBS) and insoluble (GuHCl) hippocampal fractions by ELISA. The abundance of A β peptides rose markedly with age while the A β 42:A β 40 ratio declined, particularly in the GuHCl fraction (Fig. 5). Notably, the A β 42:A β 40 ratio was higher in PS2APP;Trem2^{ko} than in PS2APP;Trem2^{wt} brains, in both TBS and GuHCl fractions across ages (Fig. 5A,B). The elevated A β 42:A β 40 ratio in PS2APP;Trem2^{ko} brains resulted more from reduced abundance of A β 40 than from increased abundance of A β 42 (Fig. 5-1, available at <https://doi.org/10.1523/JNEUROSCI.1871-19.2019.f5-1>), although A β 42 abundance was elevated in the 6–7 month females, coinciding with the increased plaque deposition we observed in that group (Fig. 3A). Together with our observation that total amyloid plaque is reduced in PS2APP;Trem2^{ko} brains at

later ages (Fig. 3A), these results suggest that the elevated A β 42:A β 40 ratio in *Trem2*-deficient brains may increase plaque seeding at younger ages (since A β 42 is more prone to aggregate and deposit than A β 40) (Klein, 2002) while reducing the incorporation and compaction of A β into existing plaques at older ages (since A β 40 permeates dense core structures more readily than A β 42) (Condello et al., 2015). Thus, Trem2 may both restrict the initial seeding of plaques and promote sequestration and compaction of A β into existing plaques.

To determine whether the elevated A β 42:A β 40 ratio was accompanied by altered abundance of soluble, fibrillar A β oligomers, we performed nondenaturing dot blots of hippocampal TBS homogenate supernatants from 12 month females. Using the conformation-specific OC antibody (Tomic et al., 2009), we detected significantly higher levels of soluble fibrillar A β oligomers in the soluble fraction from PS2APP;Trem2^{ko} mice (Fig. 5C,D), and we observed a positive correlation between the amount of OC⁺ fibrillar oligomers in this fraction and the A β 42:A β 40 ratio (Fig. 5E). In contrast, when we used the pan-reactive 6E10 A β antibody to detect total A β species in this fraction, the abundance trended slightly downward in PS2APP;Trem2^{ko} mice and correlated negatively with A β 42:A β 40 ratio (Fig. 5F–H). Similar respective trends were also seen when staining with the prefibrillar A β oligomer antibody A11 and pan-reactive 4G8 A β antibody (data not shown). As a control, we spotted hippocampal TBS homogenate supernatant from a PS2APP;Bace1^{ko} animal (Meilandt et al., 2019), in which soluble APP is still produced by α -cleavage while β -cleavage and thus A β production are prevented, and demonstrated that the OC antibody had minimal

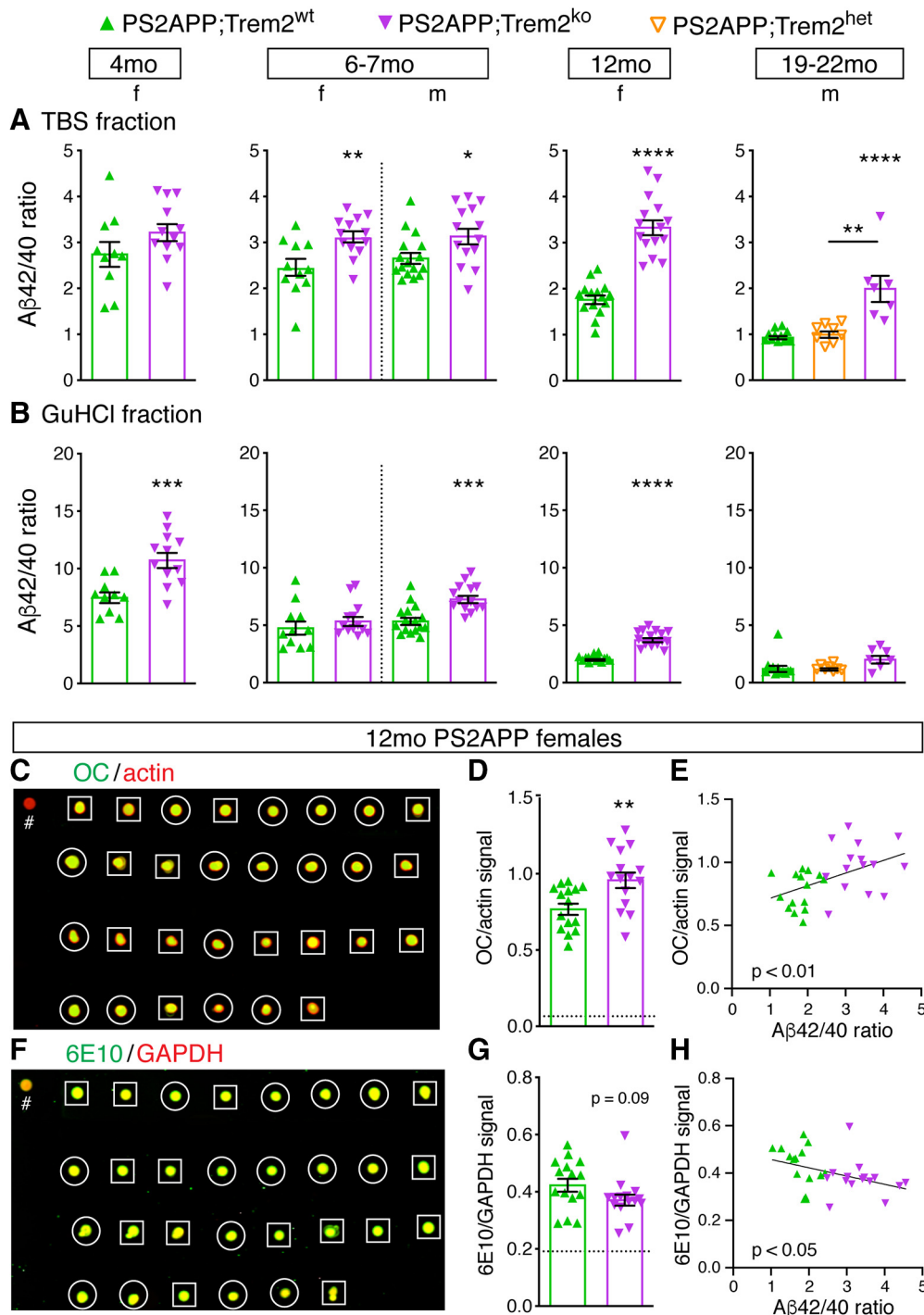


Figure 5. Trem2 deletion increases the A β 42:A β 40 ratio and soluble fibrillar A β oligomers in PS2APP brains. **A, B**, Frozen hippocampal tissues were homogenized and processed for measuring the abundance of A β 40 and A β 42 peptides by ELISA in the soluble (TBS) and insoluble (GuHCl) fractions. The ratio of A β 42:A β 40 in the TBS (**A**) and GuHCl (**B**) fractions is shown. Each data point represents 1 animal's A β 42:A β 40 ratio. For individual A β 40 and A β 42 peptide measurements, see Figure 5-1 (available at <https://doi.org/10.1523/JNEUROSCI.1871-19.2019.f5-1>). **C**, Image of nondenaturing dot blot of hippocampal soluble TBS homogenates from 12 month female animals immunostained with the fibrillar oligomeric A β antibody OC (green) and control β -actin antibody (red). Squares outline PS2APP;Trem2^{wt} samples. Circles outline PS2APP;Trem2^{ko} samples. #, Control sample from a PS2APP;Bace1^{ko} mouse. **D**, Signal intensity ratios of OC antibody to actin antibody are plotted for the dot blot shown in **C**. Dotted line indicates the OC:actin ratio for a control sample from a PS2APP;Bace1^{ko} mouse. **E**, The A β 42:A β 40 ratio (from **A**) and normalized OC⁺ dot blot signal (from **D**) in the TBS soluble fraction showed a significant positive correlation (linear regression; $df(1,28)$, $F = 8.63$, $p < 0.01$). **F**, Same as in **C**, except immunostained with pan-A β antibody 6E10 (green) and control GAPDH antibody (red). **G**, Signal intensity ratios of A β 6E10 antibody to control GAPDH antibody are plotted for the dot blot shown in **F**. The PS2APP;Bace1^{ko} control sample still has substantial 6E10 signal (see dotted line) since the N-terminal A β residues recognized by 6E10 are present in soluble APP when α -secretase is the responsible enzyme. **H**, The A β 42:A β 40 ratio (from **A**) and normalized A β 6E10 dot blot signal (from **G**) in the TBS soluble fraction showed a significant negative correlation (linear regression; $df(1,28)$, $F = 4.98$, $p < 0.05$). Error bars indicate mean \pm SEM. Unpaired *t* test or ANOVA followed by Tukey's multiple-comparison test: * $p < 0.05$, ** $p < 0.01$, *** $p < 0.001$, **** $p < 0.0001$ versus PS2APP;Trem2^{wt} or as indicated.

detection, whereas 6E10 still had substantial signal (compare # symbols in Fig. 5C,F and dotted lines in Fig. 5D,G from a PS2APP;Bace1^{ko} mouse), consistent with the ability of 6E10 to detect both soluble APP and A β peptides. These results suggest that, in the absence of Trem2, the increased A β 42:A β 40 ratio enhances the potential shift of soluble A β to a fibrillar oligomeric form. Alternatively, the increased abundance of fibrillar A β oligomers in the TBS-soluble fraction could result from reduced incorporation into highly condensed plaques in brains with Trem2-deficient microglia.

ApoE is one of the most highly induced genes in mouse microglia in response to neurodegenerative stimuli (Deczkowska et al., 2018). A recent report in the APPPS1 model found that plaque-associated ApoE was reduced in Trem2-deficient mice (Parhizkar et al., 2019). To learn whether Trem2 deletion altered ApoE localization in the PS2APP model and whether such alteration correlated with observed changes in plaque abundance, morphology, or composition, we costained for ApoE, plaques (methoxy-X04), and microglia (Iba1). In contrast to the findings of Parhizkar et al. (2019), quantification of plaque-associated ApoE in whole-brain sections found a significant increase in female PS2APP;Trem2^{ko} mice at 6–7 and 12 months of age, but no significant changes in male cohorts at any age tested (Fig. 6A). The ApoE immunostaining pattern was especially prominent in, but not limited to, the hippocampal subiculum where plaque tends to first deposit (Fig. 6B). While the incongruous results between studies may be explained by differences between mouse models, other variations in sampling and technical procedures could also account for the differences. Parhizkar et al. (2019) examined 4 month males; we only examined females at that age, and our findings of elevated plaque-associated ApoE in Trem2-deficient females were only observed at older ages. The studies used different ApoE monoclonal antibodies that likely interact with distinct epitopes or configurations of ApoE (Kim et al., 2012) and whose binding may be differentially impacted by variations in staining procedure. We immunostained for ApoE first, followed by plaque labeling, which involves treatments with ethanol and NaOH. Parhizkar et al. (2019) did the plaque labeling first, followed by the ApoE immunostains, so the nature of the ApoE at the time of immunostaining was somewhat different between studies.

Parhizkar et al. (2019) also reported that colocalization of ApoE with Iba1⁺ microglia was reduced in Trem2-deficient mice. To assess this finding in the PS2APP model, we performed confocal imaging on the ApoE/Iba1/methoxy-X04 costains from the cortex of 12 month females and again observed a contrasting result. Instead of ApoE labeling being diminished, we observed microglia in PS2APP;Trem2^{ko} mice to be markedly laden with ApoE (Fig. 6C,D), suggesting that Trem2-deficient microglia exhibit deficits in lipid clearance. At the mRNA level, we did not detect a difference in *ApoE* expression between PS2APP;Trem2^{wt} and PS2APP;Trem2^{ko} microglia (Fig. 6E; see also Fig. 2E). Although two groups have reported reductions in microglial *ApoE* expression in the APPPS1 model when Trem2 is deleted (Krasemann et al., 2017; Parhizkar et al., 2019), this does not appear to be a typical feature of Trem2 deficiency in β -amyloidosis models since previous analyses in the 5xFAD model observed Trem2-independent *ApoE* induction in either bulk microglia microarray (Fig. 6F) (Wang et al., 2015) or single-cell microglia RNA-Seq profiles (Keren-Shaul et al., 2017). In a very recent dataset of bulk microglia RNA-Seq profiles from 5xFAD mice (Griciuc et al., 2019), we did see a twofold decrease in the extent of *ApoE* induction in Trem2-deficient microglia, but the gene was still highly

induced relative to the expression level in microglia from non-transgenic mice (Fig. 6F). Together, our evidence indicates that microglial *ApoE* expression is induced by A β -driven neuropathology in a largely Trem2-independent manner, and that Trem2-deficient microglia accumulate disproportionately large amounts of ApoE compared with the smaller ApoE puncta observed in normal PS2APP microglia (Fig. 6C).

Axonal dystrophy, dendritic spine loss, and CSF NfL detection are exacerbated in PS2APP;Trem2^{ko} mice

The elevated A β 42:A β 40 ratio and fibrillar A β oligomers in PS2APP;Trem2^{ko} brains would seem to be detrimental for neuronal health since A β 42 oligomers are commonly understood to be the more toxic form of A β (Klein, 2002; Haass and Selkoe, 2007). Alternatively, the reduced plaque load in aged Trem2^{ko} brains suggested a possible benefit of Trem2 deficiency. Therefore, we turned to measures of neuronal dystrophy to better understand the potential consequences of loss of Trem2 function.

First, we looked at neuritic dystrophy around plaque (D'Amore et al., 2003) by fluorescent costaining using methoxy-X04 to label plaque, anti-Iba1 to label microglia, and anti-Lamp1 to label dystrophic axons (Gowrishankar et al., 2015) (Fig. 7A). The methoxy-X04/Iba1 costain showed that microglial association with plaque was severely compromised in PS2APP;Trem2^{ko} brains at all examined ages (Fig. 7A,B), corroborating our earlier Iba1 immunohistochemical stains that measured microglial clustering. The Lamp1 immunolabeling, which stains dilated dystrophic axons, revealed two important findings. First, on a per plaque basis, axonal dystrophy was exacerbated from 7 months onward in PS2APP;Trem2^{ko} mice (Fig. 7C), similar to findings in other β -amyloid models (Wang et al., 2016; Yuan et al., 2016). This is consistent with the idea that the diffuse plaque structures and elevated A β 42:A β 40 ratio in Trem2^{ko} brains are more damaging to surrounding axons than the more compacted, A β 40-enriched plaques in PS2APP;Trem2^{wt} brains. Second, the total Lamp1⁺ area was also increased from 7 months onward in PS2APP;Trem2^{ko} brain sections (Fig. 7D), indicating that total axonal damage was exacerbated at later ages despite the reduced plaque burden. These data strongly suggest that the Trem2-dependent clustering of microglia and their functions around plaque serve to mitigate the neurotoxic effects of A β .

Another method we used to visualize neuronal pathology was an amino-cupric-silver stain or “disintegrative degeneration” stain that labels damaged or degenerating neurons (de Olmos et al., 1994; Switzer, 2000). Overall, the staining pattern appeared very similar to the Lamp1 stain, with “bouquets” of argyrophilic structures presumably surrounding plaques throughout the cortex and hippocampus. Staining was also observed in relevant white matter tracts, such as the corpus callosum, perforant path, and fornix, suggesting that degenerating axonal processes are not restricted to dystrophic neurites around plaques. Degenerating neurites detected by this stain were more abundant in PS2APP;Trem2^{ko} brains of the 12 month female and 19–22 month male cohorts (Fig. 8A,B). Thus, again, axonal damage was exacerbated in Trem2-deficient mice from older ages despite the fact that plaque accumulation was reduced. The intermediate effect of Trem2 heterozygosity on microglial clustering around plaque (Figs. 1A, 7B) and Campbell-Switzer plaque staining (Fig. 3A), but not on plaque diffuseness (Fig. 4B), A β 42:A β 40 ratio (Fig. 5A), or neuritic dystrophy (Figs. 7C,D, 8A), suggested that the form rather than the amount of plaque correlates with neuronal damage, and that sufficient microgliosis occurs in PS2APP;Trem2^{het} mice to enable plaque compaction and neuroprotection.

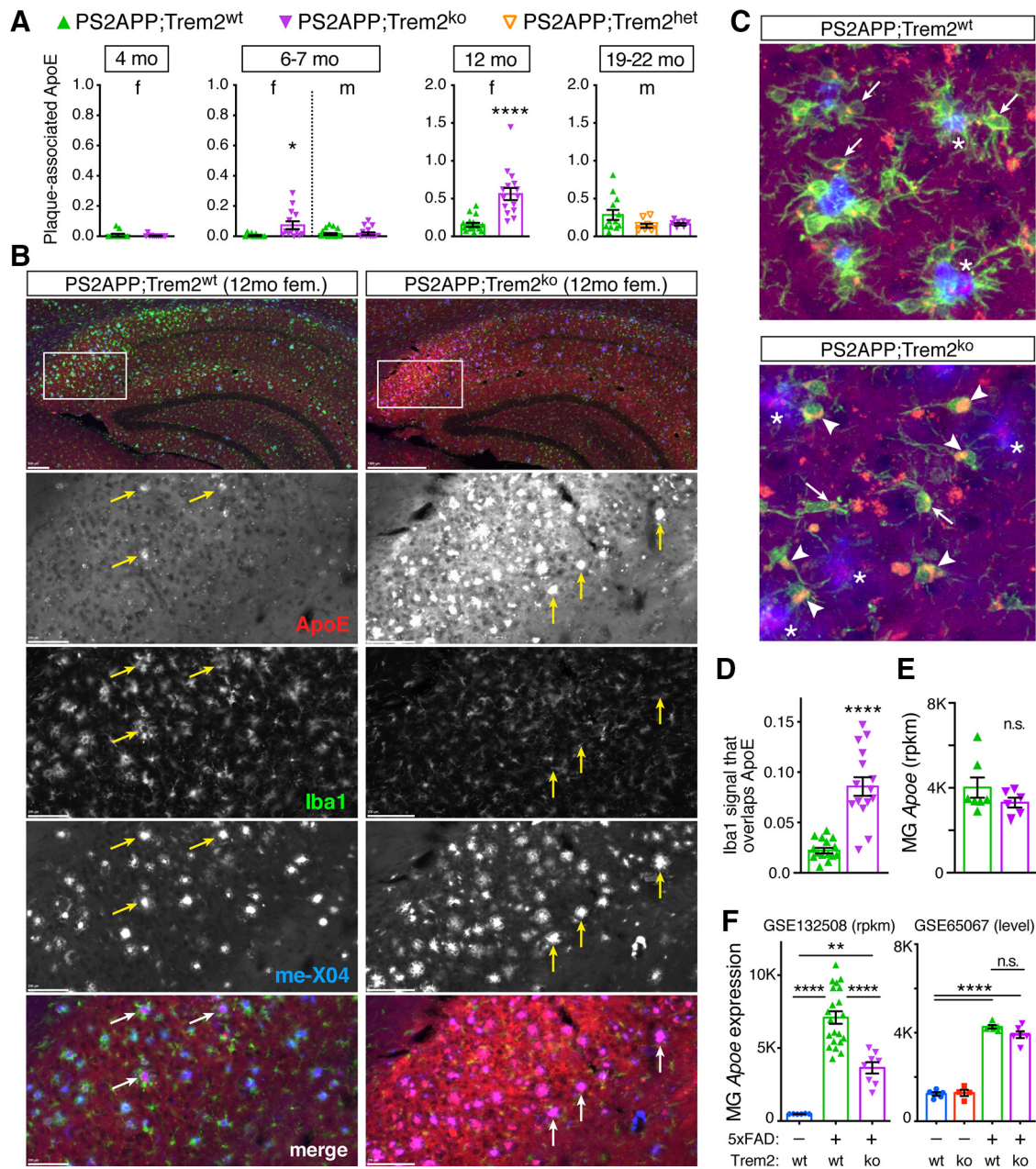


Figure 6. ApoE markedly accumulates on plaques and in microglia in PS2APP;Trem2^{ko} females. **A**, Plaque-associated ApoE signal was quantified for each animal in each cohort using 2 or 3 sections per animal, with each section having a range of ~50–800 plaques contributing to the analysis. Significant increases were observed in 6–7 month and 12 month female (f) PS2APP;Trem2^{ko} mice, but not in males (m). **B**, Representative low-magnification images of the hippocampus (top row) and high-magnification images of the subiculum (enlarged from the boxed regions) from 12 month female brain sections stained with methoxy-X04 to label plaque (blue), anti-Iba1 to label microglia (green), and anti-ApoE (red). Arrows point to examples of plaques with intense ApoE staining, which are atypical in Trem2^{wt} females but typical in Trem2^{ko} females at this age. **C**, Representative 20× maximum projection of confocal z-stacks imaged from cortex, highlighting ApoE (red) localization in microglia (Iba1, green) and plaque (blue). Microglia with small ApoE puncta (arrows) are typical in Trem2^{wt}, whereas microglia with enlarged ApoE structures (arrowheads) are frequent in Trem2^{ko}. Plaques with strong ApoE labeling are more common in Trem2^{ko} (asterisks). **D**, Analysis of the fraction of Iba1 signal that overlaps with ApoE staining (Mander’s colocalization coefficient) in 12 month PS2APP females revealed increased colocalization in Trem2^{ko} microglia. **E**, RNA-Seq profiles of microglia FACS-purified from brains of 14 month PS2APP mice showed no difference in *ApoE* expression between Trem2^{wt} and Trem2^{ko} microglia (MG). **F**, Expression profiles of microglia FACS-purified from brains of 8 month nontransgenic or 5xFAD mice revealed strong *ApoE* induction by β-amyloid pathology in both Trem2^{wt} and Trem2^{ko} microglia, with induction in 5xFAD;Trem2^{ko} relative to 5xFAD;Trem2^{wt} microglia being twofold reduced in one dataset (GSE132508, RNA-Seq) and not significantly different in another (GSE65067, microarray). Error bars indicate mean ± SEM. Unpaired *t* test or ANOVA followed by Tukey’s multiple-comparison test. **p* < 0.05, ***p* < 0.01, *****p* < 0.0001 versus PS2APP;Trem2^{wt} or as indicated. n.s. - not significant.

NfL measured in the CSF or plasma has recently emerged as a potential biomarker of neurodegeneration in human patients and in mouse disease models (Bacioglu et al., 2016; Khalil et al., 2018). To determine whether *Trem2* deficiency altered NfL levels, we collected plasma and CSF from a separate, mixed sex cohort of 12 month PS2APP;Trem2^{wt} and PS2APP;Trem2^{ko} mice.

PS2APP;Trem2^{ko} mice had significantly greater NfL levels in the CSF compared with PS2APP;Trem2^{wt} mice (Fig. 8C), consistent with the measures of increased axonal dystrophy that were observed by histopathology in *Trem2*-deficient females at this age. Perhaps surprisingly, we did not observe a difference in plasma NfL levels between genotypes (Fig. 8C), suggesting that CSF NfL

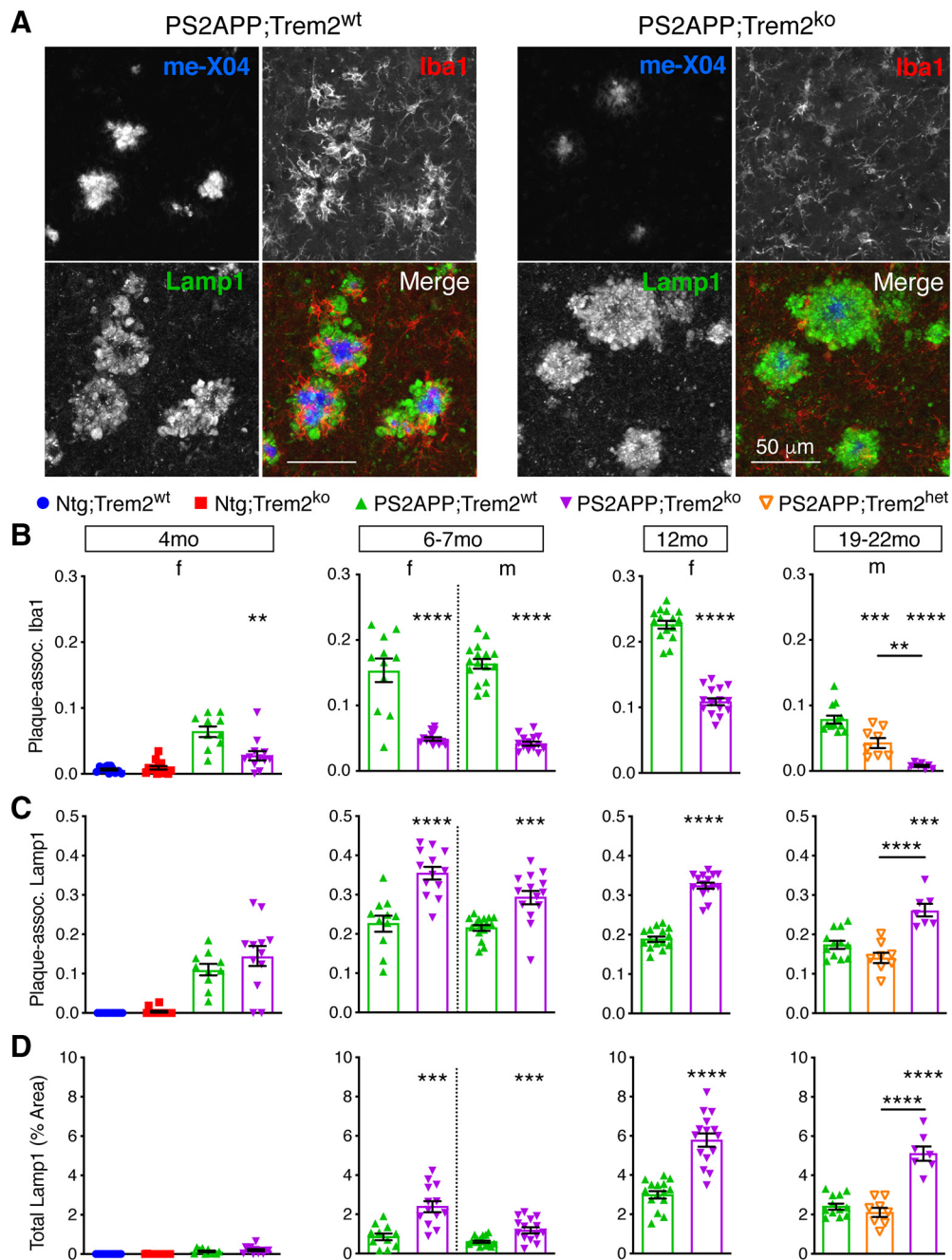


Figure 7. *Trem2* deletion exacerbates plaque-proximal axonal dystrophy. **A**, Representative images from 12 month brain sections stained with methoxy-X04 to label plaque, anti-Iba1 to label microglia, and anti-Lamp1 to label dystrophic axons around plaque. **B**, Microglial clustering around plaque is impaired in *Trem2*-deficient mice. Plaque-associated Iba1 signal was quantified for each animal in each cohort using 2 or 3 sections per animal, with each section having hundreds or thousands of plaques contributing to the analysis. **C**, Axonal dystrophy per plaque is exacerbated in *Trem2*-deficient mice. Plaque-associated Lamp1 signal was quantified for each animal in a similar manner as Iba1 signal in **B**. **D**, Total axonal dystrophy is exacerbated in *Trem2*-deficient mice. Total Lamp1 signal in each section was quantified, and each data point represents the average score from 2 or 3 sections per animal. Error bars indicate mean \pm SEM. Unpaired *t* test or ANOVA followed by Tukey's multiple-comparison test. ***p* < 0.01, ****p* < 0.001, *****p* < 0.0001 versus PS2APP;Trem2^{wt} or as indicated.

measurements better represent ongoing neuronal damage or degeneration in the CNS than plasma measurements.

Finally, we looked at whether another feature of neuronal pathology observed in AD tissues and β -amyloid mouse models, reduced synaptic density, particularly near plaque (Spire and Hyman, 2004; Tsai et al., 2004; Spire et al., 2005), was altered in *Trem2*-deficient mice. In β -amyloid models, the reduction in synapse number requires the presence of microglia since depleting the microglial cell population largely prevents loss of synaptic density (Olmos-Alonso et al., 2016; Spangenberg et al., 2016).

Therefore, we asked whether *Trem2* deletion and the resulting lack of activated, plaque-associated microglia would prevent the dendritic spine loss from occurring or would worsen it. To answer this, we crossed the Thy1:GFP-M line, which labels a sparse population of excitatory neurons, into the PS2APP model and analyzed a cohort of 6 month female mice with different *Trem2* genotypes. Spine density loss in the proximity of plaques was not rescued by *Trem2* deletion, but was actually further exacerbated in PS2APP;Trem2^{ko} mice compared with PS2APP;Trem2^{wt} or PS2APP;Trem2^{het} groups (Fig. 9). Thus, *Trem2* is not required

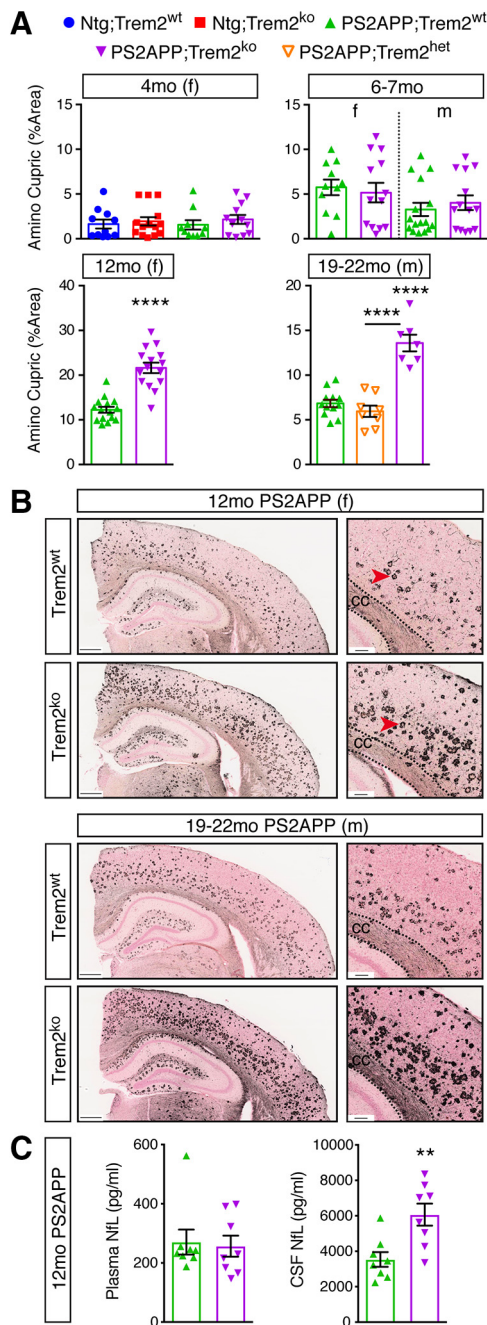


Figure 8. Disintegrative degeneration staining and CSF NfL measurements reveal exacerbated neuronal damage in *Trem2*-deficient mice at later ages. **A**, Quantification of sections from nontransgenic (Ntg) and PS2APP mice with indicated *Trem2* genotypes stained using an amino cupric silver staining method that labels degenerative neuronal processes. Each data point represents the average percent area covered/section for ~10 sections per animal. **B**, Representative low (left, scale bar, 400 μ m) and high (right, scale bar, 100 μ m) magnification images from the 12 month female and 19–22 month male cohorts are shown. Degenerative signal is apparent in plaque-accompanying foci (red arrowheads) throughout the cortex and hippocampus and in certain white matter tracts, including the corpus callosum (cc). **C**, Plasma (left) and CSF (right) NfL were measured from a separate, mixed sex cohort of 12 months PS2APP; *Trem2*^{wt} and PS2APP; *Trem2*^{ko} mice. Error bars indicate mean \pm SEM. Unpaired *t* test or ANOVA followed by Tukey’s multiple-comparison test: ***p* < 0.01, *****p* < 0.0001 versus PS2APP; *Trem2*^{wt} or as indicated.

for microglia-mediated dendritic spine loss around plaque; and indeed, *Trem2* seems to hedge against synapse loss. Overall, the exacerbated axonal dystrophy and dendritic spine loss observed around plaque in PS2APP; *Trem2*^{ko} mice imply that *Trem2*-

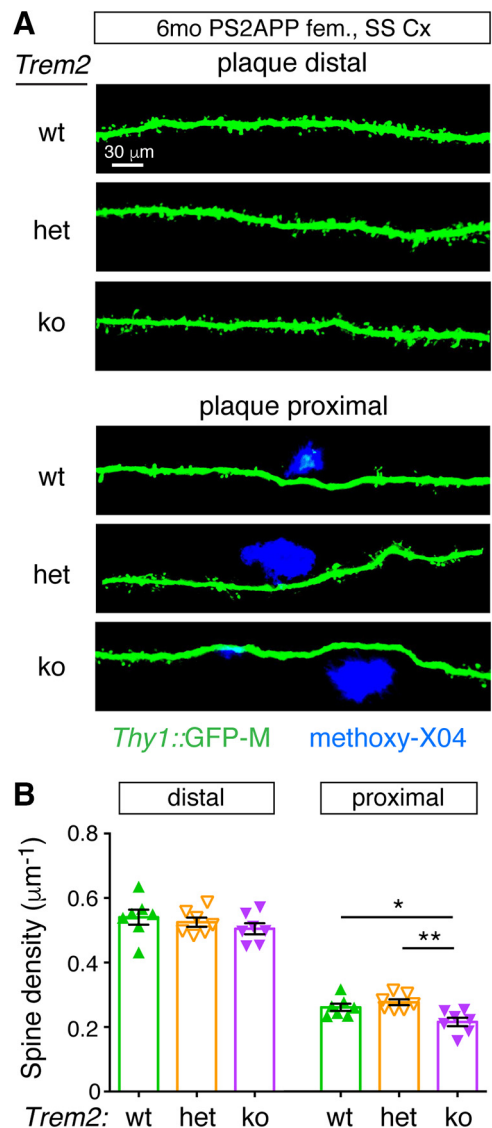


Figure 9. *Trem2* deletion exacerbates dendritic spine loss near plaque. **A**, Intact brains from 6 month female PS2APP mice with WT (wt), KO (ko), or heterozygous (het) *Trem2* genotypes and carrying the Thy1::GFP-M transgene, which sparsely labels excitatory cortical neurons, were imaged in the somatosensory cortex (SS Cx) using two-photon microscopy. Dendritic shafts proximal to plaque (within 20 μ m) or distally located (\geq 100 μ m from any plaque) were imaged, with representative images shown. **B**, Each data point represents the average of five spine density measurements from 1 animal. Spine density was ~50% reduced on plaque-proximal dendrite segments relative to distal dendrite segments from the same animals. Spine density near plaque was lower in PS2APP; *Trem2*^{ko} mice than in PS2APP; *Trem2*^{wt} or PS2APP; *Trem2*^{het} mice. Error bars indicate mean \pm SEM. ANOVA: **p* < 0.05, ***p* < 0.01. Spine volume was unaffected by either plaque proximity or *Trem2* genotype (data not shown).

dependent microglial activity is fundamentally neuroprotective in β -amyloid-driven models of AD-like pathology.

Discussion

In this study, we examined the role of *Trem2* in microglial activation, plaque accumulation, and neuronal dystrophy in the PS2APP model of β -amyloidosis. We observed both age- and sex-dependent effects of *Trem2* deletion on plaque abundance assessed using the Campbell-Switzer silver stain, with slightly more plaque in PS2APP; *Trem2*^{ko} females at 6–7 months of age but markedly less plaque in both female and male PS2APP; *Trem2*^{ko} mice at later ages. Together with a recent similar report

(Parhizkar et al., 2019), these results suggest that Trem2-dependent microglial activity may both restrain the formation/seeding of plaques at an early stage of pathology, conceivably through uptake and degradation of soluble A β species, but also enhance the sequestration of A β into existing plaque structures, particularly at later stages of pathology.

At all ages examined, and in both sexes, microglial clustering around plaque and other measurements of microglial activation were sharply reduced in PS2APP;Trem2^{ko} mice. Transcriptional induction of the neurodegeneration-related modules, the proliferation module, and certain genes related to Wnt regulation were impaired in PS2APP;Trem2^{ko} microglia. Presumably as a consequence of the impaired microglial response around plaque, plaques in PS2APP;Trem2^{ko} brains displayed a more diffuse morphology than in PS2APP;Trem2^{wt} brains. From 6–7 months onward, axonal injury was magnified in PS2APP;Trem2^{ko} mice, even at later ages when the abundance of argyrophilic amyloid plaques was diminished. Our finding that plaque-proximal dendritic spine loss was exacerbated in PS2APP;Trem2^{ko} mice further underscored that the Trem2-dependent microglial activation around plaque is protective for neurons and is distinct from microglia-mediated, complement-mediated activities that contribute to synapse loss in β -amyloid models (Fonseca et al., 2004; Hong et al., 2016; Shi et al., 2017; Wu et al., 2019). It will be important for future studies of microglial modulation in mouse models to analyze plaque-associated neuritic dystrophy and not assume that decreases (or increases) in amyloid plaque burden are evidence of beneficial (or detrimental) effects.

While the elevated A β ₄₂:A β ₄₀ ratio we observed in the soluble fraction of PS2APP;Trem2^{ko} brains could reflect direct deficits in the Trem2-mediated binding and clearance of oligomeric A β ₄₂ by microglia (Yeh et al., 2016; Lessard et al., 2018; Zhao et al., 2018), it could also reflect enhanced clearance of A β ₄₀ through other means, such as vascular efflux. The resulting elevation in soluble A β ₄₂:A β ₄₀ ratio may give rise to the increased plaque formation we observed in 6–7 month females, similar to the increased plaque seeding activity observed by others at a similar age in another model when Trem2 was deleted (Parhizkar et al., 2019). Given that A β ₄₀ is more easily incorporated into existing dense plaque structures than A β ₄₂ (Condello et al., 2015), our observation that the A β ₄₂:A β ₄₀ ratio declines as the mice age, particularly in the insoluble fraction, is consistent with the accumulation of compact plaques in size and number over time in the brains of PS2APP mice. The reduction of this plaque accumulation activity in PS2APP;Trem2^{ko} brains may underlie the elevated levels of fibrillar oligomeric A β we detected in the soluble fraction, which may in turn be a source of increased neuronal injury in these animals.

The weakness of correlation between plaque abundance and cognitive status in humans, along with several unsuccessful clinical trials aimed at preventing cognitive decline by reducing brain A β levels, has led some to question the relevance of A β in the etiology and progression of AD (Krstic and Knuesel, 2013; Morris et al., 2014; Itzhaki et al., 2016). Moreover, many have proposed that chronic microglial activation is a key damaging agent that contributes to the neurotoxic environment in AD (Heneka et al., 2015; Park et al., 2018). Our results suggest the opposite, since preventing the microglial response to A β pathology via Trem2 deletion reversed neither axonal dystrophy nor dendritic spine loss around plaque and indeed made both of these pathologies worse. Trem2 deletion also increased the amount of NfL detected in CSF. Evidence in humans and mice supports the mechanistic model that β -amyloid pathology accelerates the accumulation of

tau pathology or enhances its spreading (Pooler et al., 2015; He et al., 2018; Jack et al., 2018; Jacobs et al., 2018), and a new report indicates that this effect is further magnified in Trem2-deficient mice (Leyns et al., 2019). Together, these findings suggest that the form of microglial activation brought on by A β -related pathologies (the DAM state, or at least the Trem2-dependent component of it) protects neurons by limiting A β -induced neuronal injury.

Supporting the notion that microglial activation is primarily beneficial in the context of AD pathology, elevated PET signal for ligands of the “neuroinflammation marker” TSPO have predicted better cognitive measures and slower AD progression in mice with β -amyloid pathology and human patients, respectively (Hamelin et al., 2016; Focke et al., 2019). The fact that plaques in Trem2-deficient mice are more injurious to adjacent neurites but show weaker labeling with molecular probes (Thioflavin S, methoxy-X04 and X-34) related to those used in the clinic (¹¹C-PiB, ¹⁸F-Florbetapir) helps explain why cognitive decline correlates better with tau pathology and synapse loss than with brain amyloid detection. The form of β -amyloid in the brain is more critical than the amount, and Trem2-mediated microgliosis facilitates the consolidation of β -amyloid into a highly compacted, less damaging form. Therefore, therapeutics that enhance this microglial activity may prevent AD or delay its progression while simultaneously (and perhaps counterintuitively) leading to increases in PET signals for amyloid content and microgliosis. Clinical biomarkers of neuronal degeneration and spreading AD pathology, such as neurofilament-L and tau, should be more informative indicators of whether a microglia-directed therapy is achieving efficacy.

References

- Andorfer C, Kress Y, Espinoza M, de Silva R, Tucker KL, Barde YA, Duff K, Davies P (2003) Hyperphosphorylation and aggregation of tau in mice expressing normal human tau isoforms. *J Neurochem* 86:582–590.
- Bacioglu M, Maia LF, Preische O, Schelle J, Apel A, Kaeser SA, Schweighauser M, Eninger T, Lambert M, Pilotto A, Shimshek DR, Neumann U, Kahle PJ, Staufenbiel M, Neumann M, Maetzler W, Kuhle J, Jucker M (2016) Neurofilament light chain in blood and CSF as marker of disease progression in mouse models and in neurodegenerative diseases. *Neuron* 91:56–66.
- Bemiller SM, McCray TJ, Allan K, Formica SV, Xu G, Wilson G, Kokiko-Cochran ON, Crish SD, Lasagna-Reeves CA, Ransohoff RM, Landreth GE, Lamb BT (2017) TREM2 deficiency exacerbates tau pathology through dysregulated kinase signaling in a mouse model of tauopathy. *Mol Neurodegener* 12:74.
- Berger H, Wodarz A, Borchers A (2017) PTK7 faces the wnt in development and disease. *Front Cell Dev Biol* 5:31.
- Boerboom D, White LD, Dalle S, Courty J, Richards JS (2006) Dominant-stable beta-catenin expression causes cell fate alterations and wnt signaling antagonist expression in a murine granulosa cell tumor model. *Cancer Res* 66:1964–1973.
- Bouchon A, Hernández-Munain C, Cella M, Colonna M (2001) A DAP12-mediated pathway regulates expression of CC chemokine receptor 7 and maturation of human dendritic cells. *J Exp Med* 194:1111–1122.
- Buchman JJ, Durak O, Tsai LH (2011) ASPM regulates wnt signaling pathway activity in the developing brain. *Genes Dev* 25:1909–1914.
- Busby V, Goossens S, Nowotny P, Hamilton G, Smemo S, Harold D, Turic D, Jehu L, Myers A, Womick M, Woo D, Compton D, Doil LM, Tacey KM, Lau KF, Al-Saraj S, Killick R, Pickering-Brown S, Moore P, Hollingworth P, et al. (2004) Alpha-T-catenin is expressed in human brain and interacts with the wnt signaling pathway but is not responsible for linkage to chromosome 10 in Alzheimer’s disease. *Neuromolecular Med* 5:133–146.
- Campbell SK, Switzer RC, Martin TL (1987) Alzheimer’s plaques and tangles: a controlled and enhanced silver staining method. *Soc Neuroscience Abstr* 13:678.
- Cella M, Buonsanti C, Strader C, Kondo T, Salmaggi A, Colonna M (2003) Impaired differentiation of osteoclasts in TREM-2-deficient individuals. *J Exp Med* 198:645–651.

- Condello C, Yuan P, Schain A, Grutzendler J (2015) Microglia constitute a barrier that prevents neurotoxic protofibrillar A β 42 hotspots around plaques. *Nat Commun* 6:6176.
- D'Amore JD, Kajdasz ST, McLellan ME, Bacskai BJ, Stern EA, Hyman BT (2003) In vivo multiphoton imaging of a transgenic mouse model of Alzheimer disease reveals marked thioflavine-S-associated alterations in neurite trajectories. *J Neuropathol Exp Neurol* 62:137–145.
- Deczkowska A, Keren-Shaul H, Weiner A, Colonna M, Schwartz M, Amit I (2018) Disease-associated microglia: a universal immune sensor of neurodegeneration. *Cell* 173:1073–1081.
- de Olmos JS, Beltramo CA, de Olmos de Lorenzo S (1994) Use of an amino-cupric-silver technique for the detection of early and semiacute neuronal degeneration caused by neurotoxicants, hypoxia, and physical trauma. *Neurotoxicol Teratol* 16:545–561.
- Devotta A, Hong CS, Saint-Jeannet JP (2018) Dkk2 promotes neural crest specification by activating Wnt/ β -catenin signaling in a GSK3 β independent manner. *Elife* 7:e34404.
- Diep DB, Hoen N, Backman M, Machon O, Krauss S (2004) Characterisation of the wnt antagonists and their response to conditionally activated wnt signalling in the developing mouse forebrain. *Brain Res Dev Brain Res* 153:261–270.
- Diks SH, Bink RJ, van de Water S, Joore J, van Rooijen C, Verbeek FJ, den Hertog J, Peppelenbosch MP, Zivkovic D (2006) The novel gene asb11: a regulator of the size of the neural progenitor compartment. *J Cell Biol* 174:581–592.
- Dunn KW, Kamocka MM, McDonald JH (2011) A practical guide to evaluating colocalization in biological microscopy. *Am J Physiol Cell Physiol* 300:C723–C742.
- Focke C, Blume T, Zott B, Shi Y, Deussing M, Peters F, Schmidt C, Kleinberger G, Lindner S, Gildehaus FJ, Beyer L, von Ungern-Sternberg B, Bartenstein P, Ozmen L, Baumann K, Dorostkar MM, Haass C, Adelsberger H, Herms J, Rominger A, et al. (2019) Early and longitudinal microglial activation but not amyloid accumulation predicts cognitive outcome in PS2APP mice. *J Nucl Med* 60:548–554.
- Fonseca MI, Zhou J, Botto M, Tenner AJ (2004) Absence of C1q leads to less neuropathology in transgenic mouse models of Alzheimer's disease. *J Neurosci* 24:6457–6465.
- Friedman BA, Srinivasan K, Ayalon G, Meilandt WJ, Lin H, Huntley MA, Cao Y, Lee SH, Haddick PC, Ngu H, Modrusan Z, Larson JL, Kaminker JS, van der Brug MP, Hansen DV (2018) Diverse brain myeloid expression profiles reveal distinct microglial activation states and aspects of Alzheimer's disease not evident in mouse models. *Cell Rep* 22:832–847.
- Gage PJ, Qian M, Wu D, Rosenberg KI (2008) The canonical wnt signaling antagonist DKK2 is an essential effector of PITX2 function during normal eye development. *Dev Biol* 317:310–324.
- Gowrishankar S, Yuan P, Wu Y, Schrag M, Paradise S, Grutzendler J, De Camilli P, Ferguson SM (2015) Massive accumulation of luminal protease-deficient axonal lysosomes at Alzheimer's disease amyloid plaques. *Proc Natl Acad Sci U S A* 112:E3699–E3708.
- Gratuzze M, Leyns CE, Holtzman DM (2018) New insights into the role of TREM2 in Alzheimer's disease. *Mol Neurodegener* 13:66.
- Griuciu A, Patel S, Federico AN, Choi SH, Innes BJ, Oram MK, Cereghetti G, McGinty D, Anselmo A, Sadeyev RI, Hickman SE, El Khoury J, Colonna M, Tanzi RE (2019) TREM2 acts downstream of CD33 in modulating microglial pathology in Alzheimer's disease. *Neuron* 103:820–835.e7.
- Guerreiro R, Wojtas A, Bras J, Carrasquillo M, Rogava E, Majounie E, Cruchaga C, Sassi C, Kauwe JS, Younkin S, Hazrati L, Collinge J, Pocock J, Lashley T, Williams J, Lambert JC, Amouyel P, Goate A, Rademakers R, Morgan K, et al. (2013) TREM2 variants in Alzheimer's disease. *N Engl J Med* 368:117–127.
- Haass C, Selkoe DJ (2007) Soluble protein oligomers in neurodegeneration: lessons from the Alzheimer's amyloid β -peptide. *Nat Rev Mol Cell Biol* 8:101–112.
- Hamelin L, Lagarde J, Dorothée G, Leroy C, Labit M, Comley RA, de Souza LC, Corne H, Dauphinot L, Bertoux M, Dubois B, Gervais P, Colliot O, Potier MC, Bottlaender M, Sarazin M (2016) Early and protective microglial activation in Alzheimer's disease: a prospective study using 18F-DPA-714 PET imaging. *Brain* 139:1252–1264.
- Hansen DV, Hanson JE, Sheng M (2018) Microglia in Alzheimer's disease. *J Cell Biol* 217:459–472.
- He Z, Guo JL, McBride JD, Narasimhan S, Kim H, Changolkar L, Zhang B, Gathagan RJ, Yue C, Dengler C, Stieber A, Nidla M, Coulter DA, Abel T, Brunden KR, Trojanowski JQ, Lee VM (2018) Amyloid- β plaques enhance Alzheimer's brain tau-seeded pathologies by facilitating neuritic plaque tau aggregation. *Nat Med* 24:29–38.
- Heneka MT, Carson MJ, El Khoury J, Landreth GE, Brosseron F, Feinstein DL, Jacobs AH, Wyss-Coray T, Vitorica J, Ransohoff RM, Herrup K, Frautschy SA, Finsen B, Brown GC, Verkhratsky A, Yamanaka K, Koistinaho J, Latz E, Halle A, Petzold GC, et al. (2015) Neuroinflammation in Alzheimer's disease. *Lancet Neurol* 14:388–405.
- Hong S, Beja-Glasser VF, Nfonoyim BM, Frouin A, Li S, Ramakrishnan S, Merry KM, Shi Q, Rosenthal A, Barres BA, Lemere CA, Selkoe DJ, Stevens B (2016) Complement and microglia mediate early synapse loss in Alzheimer mouse models. *Science* 352:712–716.
- Hsieh JC, Kodjabachian L, Rebertus ML, Rattner A, Smallwood PM, Samos CH, Nusse R, Dawid IB, Nathans J (1999) A new secreted protein that binds to wnt proteins and inhibits their activities. *Nature* 398:431–436.
- Itzhaki RF, Lathe R, Balin BJ, Ball MJ, Bearer EL, Braak H, Bullido MJ, Carter C, Clerici M, Cosby SL, Del Tredici K, Field H, Fulop T, Grassi C, Griffin WS, Haas J, Hudson AP, Kamer AR, Kell DB, Licastro F, et al. (2016) Microbes and Alzheimer's disease. *J Alzheimers Dis* 51:979–984.
- Jack CR Jr, Wiste HJ, Schwarz CG, Lowe VJ, Senjem ML, Vemuri P, Weigand SD, Therneau TM, Knopman DS, Gunter JL, Jones DT, Graff-Radford J, Kantarci K, Roberts RO, Mielke MM, Machulda MM, Petersen RC (2018) Longitudinal tau PET in ageing and Alzheimer's disease. *Brain* 141:1517–1528.
- Jacobs HI, Hedden T, Schultz AP, Sepulcre J, Perea RD, Amariglio RE, Papp KV, Rentz DM, Sperling RA, Johnson KA (2018) Structural tract alterations predict downstream tau accumulation in amyloid-positive older individuals. *Nat Neurosci* 21:424–431.
- Jay TR, Miller CM, Cheng PJ, Graham LC, Bemiller S, Broihier ML, Xu G, Margevicius D, Karlo JC, Sousa GL, Cotleur AC, Butovsky O, Bekris L, Staugaitis SM, Leverenz JB, Pimprikar SW, Landreth GE, Howell GR, Ransohoff RM, Lamb BT (2015) TREM2 deficiency eliminates TREM2⁺ inflammatory macrophages and ameliorates pathology in Alzheimer's disease mouse models. *J Exp Med* 212:287–295.
- Jay TR, Hirsch AM, Broihier ML, Miller CM, Neilson LE, Ransohoff RM, Lamb BT, Landreth GE (2017a) Disease progression-dependent effects of TREM2 deficiency in a mouse model of Alzheimer's disease. *J Neurosci* 37:637–647.
- Jay TR, von Saucken VE, Landreth GE (2017b) TREM2 in neurodegenerative diseases. *Mol Neurodegener* 12:56.
- Jonsson T, Stefansson H, Steinberg S, Jonsson I, Jonsson PV, Snaedal J, Bjornsson S, Huttenlocher J, Levey AI, Lah JJ, Rujescu D, Hampel H, Giegling I, Andreassen OA, Engedal K, Ulstein I, Djurovic S, Ibrahim-Verbaas C, Hofman A, Ikram MA, et al. (2013) Variant of TREM2 associated with the risk of Alzheimer's disease. *N Engl J Med* 368:107–116.
- Kallop DY, Meilandt WJ, Gogineni A, Easley-Neal C, Wu T, Jubb AM, Yaylaoglu M, Shamloo M, Tessier-Lavigne M, Scarce-Lavie K, Weimer RM (2014) A death receptor 6-amyloid precursor protein pathway regulates synapse density in the mature CNS but does not contribute to Alzheimer's disease-related pathophysiology in murine models. *J Neurosci* 34:6425–6437.
- Kang SS, Kurti A, Baker KE, Liu CC, Colonna M, Ulrich JD, Holtzman DM, Bu G, Fryer JD (2018) Behavioral and transcriptomic analysis of Trem2-null mice: not all knockout mice are created equal. *Hum Mol Genet* 27:211–223.
- Karasawa T, Yokokura H, Kitajewski J, Lombroso PJ (2002) Frizzled-9 is activated by wnt-2 and functions in Wnt/ β -catenin signaling. *J Biol Chem* 277:37479–37486.
- Keren-Shaul H, Spinrad A, Weiner A, Matcovitch-Natan O, Dvir-Szternfeld R, Ulland TK, David E, Baruch K, Lara-Astaiso D, Toth B, Itzkovitz S, Colonna M, Schwartz M, Amit I (2017) A unique microglia type associated with restricting development of Alzheimer's disease. *Cell* 169:1276–1290.e17.
- Khalil M, Teunissen CE, Otto M, Piehl F, Sormani MP, Gattlinger T, Barro C, Kappos L, Comabella M, Fazekas F, Petzold A, Blennow K, Zetterberg H, Kuhle J (2018) Neurofilaments as biomarkers in neurological disorders. *Nat Rev Neurol* 14:577–589.
- Kim J, Eltorai AE, Jiang H, Liao F, Verghese PB, Kim J, Stewart FR, Basak JM, Holtzman DM (2012) Anti-apoE immunotherapy inhibits amyloid accumulation in a transgenic mouse model of abeta amyloidosis. *J Exp Med* 209:2149–2156.

- Klein WL (2002) Abeta toxicity in Alzheimer's disease: globular oligomers (ADDLs) as new vaccine and drug targets. *Neurochem Int* 41:345–352.
- Glunk WE, Bacskai BJ, Mathis CA, Kajdasz ST, McLellan ME, Frosch MP, Debnath ML, Holt DP, Wang Y, Hyman BT (2002) Imaging abeta plaques in living transgenic mice with multiphoton microscopy and methoxy-X04, a systemically administered Congo red derivative. *J Neuropathol Exp Neurol* 61:797–805.
- Krasemann S, Madore C, Cialic R, Baufeld C, Calcagno N, El Fatimy R, Beckers L, O'Loughlin E, Xu Y, Fanek Z, Greco DJ, Smith ST, Tweet G, Humulock Z, Zrzavy T, Conde-Sanroman P, Gacias M, Weng Z, Chen H, Tjon E, et al. (2017) The TREM2-APOE pathway drives the transcriptional phenotype of dysfunctional microglia in neurodegenerative diseases. *Immunity* 47:566–581.e9.
- Krstic D, Knuesel I (2013) The airbag problem—a potential culprit for bench-to-bedside translational efforts: relevance for Alzheimer's disease. *Acta Neuropathol Commun* 1:62.
- Lai JP, Oseini AM, Moser CD, Yu C, Elsawa SF, Hu C, Nakamura I, Han T, Aderca I, Isomoto H, Garrity-Park MM, Shire AM, Li J, Sanderson SO, Adjei AA, Fernandez-Zapico ME, Roberts LR (2010) The oncogenic effect of sulfatase 2 in human hepatocellular carcinoma is mediated in part by glypican 3-dependent wnt activation. *Hepatology* 52:1680–1689.
- Law CW, Chen Y, Shi W, Smyth GK (2014) voom: precision weights unlock linear model analysis tools for RNA-seq read counts. *Genome Biol* 15:R29.
- Le Pichon CE, Dominguez SL, Solano H, Ngu H, Lewin-Koh N, Chen M, Eastham-Anderson J, Watts R, Scarce-Levie K (2013) EGFR inhibitor erlotinib delays disease progression but does not extend survival in the SOD1 mouse model of ALS. *PLoS One* 8:e62342.
- Lessard CB, Malnik SL, Zhou Y, Ladd TB, Cruz PE, Ran Y, Mahan TE, Chakrabaty P, Holtzman DM, Ulrich JD, Colonna M, Golde TE (2018) High-affinity interactions and signal transduction between Abeta oligomers and TREM2. *EMBO Mol Med* 10:e9027.
- Leyns CE, Ulrich JD, Finn MB, Stewart FR, Koscal LJ, Remolina Serrano J, Robinson GO, Anderson E, Colonna M, Holtzman DM (2017) TREM2 deficiency attenuates neuroinflammation and protects against neurodegeneration in a mouse model of tauopathy. *Proc Natl Acad Sci U S A* 114:11524–11529.
- Leyns CE, Gratzu M, Narasimhan S, Jain N, Koscal LJ, Jiang H, Manis M, Colonna M, Lee VM, Ulrich JD, Holtzman DM (2019) TREM2 function impedes tau seeding in neuritic plaques. *Nat Neurosci* 22:1217–1222.
- Lin Z, Gao C, Ning Y, He X, Wu W, Chen YG (2008) The pseudoreceptor BMP and activin membrane-bound inhibitor positively modulates Wnt/beta-catenin signaling. *J Biol Chem* 283:33053–33058.
- Love MI, Huber W, Anders S (2014) Moderated estimation of fold change and dispersion for RNA-seq data with DESeq2. *Genome Biol* 15:550.
- Mao B, Niehrs C (2003) Kremen2 modulates Dickkopf2 activity during Wnt/LRP6 signaling. *Gene* 302:179–183.
- Mazaheri F, Snaidero N, Kleinberger G, Madore C, Daria A, Werner G, Krasemann S, Capell A, Trümbach D, Wurst W, Brunner B, Bultmann S, Tahirovic S, Kerschensteiner M, Misgeld T, Butovsky O, Haass C (2017) TREM2 deficiency impairs chemotaxis and microglial responses to neuronal injury. *EMBO Rep* 18:1186–1198.
- Meilandt WJ, Maloney JA, Imperio J, Lalehzadeh G, Earr T, Crowell S, Bainbridge TW, Lu Y, Ernst JA, Fuji RN, Atwal JK (2019) Characterization of the selective in vitro and in vivo binding properties of crenezumab to oligomeric A β . *Alzheimers Res Ther* 11:97.
- Mi H, Muruganujan A, Ebert D, Huang X, Thomas PD (2019) PANTHER version 14: more genomes, a new PANTHER GO-slim and improvements in enrichment analysis tools. *Nucleic Acids Res* 47:D419–D426.
- Morris GP, Clark IA, Vissel B (2014) Inconsistencies and controversies surrounding the amyloid hypothesis of Alzheimer's disease. *Acta Neuropathol Commun* 2:135.
- Olmos-Alonso A, Schetters ST, Sri S, Askew K, Mancuso R, Vargas-Caballero M, Holscher C, Perry VH, Gomez-Nicola D (2016) Pharmacological targeting of CSF1R inhibits microglial proliferation and prevents the progression of Alzheimer's-like pathology. *Brain* 139:891–907.
- Orre M, Kamphuis W, Osborn LM, Jansen AH, Kooijman L, Bossers K, Hol EM (2014) Isolation of glia from Alzheimer's mice reveals inflammation and dysfunction. *Neurobiol Aging* 35:2746–2760.
- Ozmen L, Albientz A, Czech C, Jacobsen H (2009) Expression of transgenic APP mRNA is the key determinant for beta-amyloid deposition in PS2APP transgenic mice. *Neurodegener Dis* 6:29–36.
- Paloneva J, Mandelin J, Kiialainen A, Bohling T, Prudlo J, Hakola P, Haltia M, Kontinen YT, Peltonen L (2003) DAP12/TREM2 deficiency results in impaired osteoclast differentiation and osteoporotic features. *J Exp Med* 198:669–675.
- Parhizkar S, Arzberger T, Brendel M, Kleinberger G, Deussing M, Focke C, Nuscher B, Xiong M, Ghasemigharagoz A, Katzmarski N, Krasemann S, Lichtenthaler SF, Müller SA, Colombo A, Monasor LS, Tahirovic S, Herms J, Willem M, Pettkus N, Butovsky O, et al. (2019) Loss of TREM2 function increases amyloid seeding but reduces plaque-associated ApoE. *Nat Neurosci* 22:191–204.
- Park J, Wetzel I, Marriott I, Dréau D, D'Avanzo C, Kim DY, Tanzi RE, Cho H (2018) A 3D human triculture system modeling neurodegeneration and neuroinflammation in Alzheimer's disease. *Nat Neurosci* 21:941–951.
- Poliani PL, Wang Y, Fontana E, Robinette ML, Yamanishi Y, Gilfillan S, Colonna M (2015) TREM2 sustains microglial expansion during aging and response to demyelination. *J Clin Invest* 125:2161–2170.
- Pooler AM, Polydorou M, Maury EA, Nicholls SB, Reddy SM, Wegmann S, William C, Saqran L, Cagsal-Getkin O, Pitstick R, Beier DR, Carlson GA, Spires-Jones TL, Hyman BT (2015) Amyloid accelerates tau propagation and toxicity in a model of early Alzheimer's disease. *Acta Neuropathol Commun* 3:14.
- Shi Q, Chowdhury S, Ma R, Le KX, Hong S, Caldarone BJ, Stevens B, Lemere CA (2017) Complement C3 deficiency protects against neurodegeneration in aged plaque-rich APP/PS1 mice. *Sci Transl Med* 9:eaaf6295.
- Spangenberg EE, Lee RJ, Najafi AR, Rice RA, Elmore MR, Blurton-Jones M, West BL, Green KN (2016) Eliminating microglia in Alzheimer's mice prevents neuronal loss without modulating amyloid-beta pathology. *Brain* 139:1265–1281.
- Spires TL, Hyman BT (2004) Neuronal structure is altered by amyloid plaques. *Rev Neurosci* 15:267–278.
- Spires TL, Meyer-Luehmann M, Stern EA, McLean PJ, Skoch J, Nguyen PT, Bacskai BJ, Hyman BT (2005) Dendritic spine abnormalities in amyloid precursor protein transgenic mice demonstrated by gene transfer and intravital multiphoton microscopy. *J Neurosci* 25:7278–7287.
- Srinivasan K, Friedman BA, Larson JL, Lauffer BE, Goldstein LD, Appling LL, Borneo J, Poon C, Ho T, Cai F, Steiner P, van der Brug MP, Modrusan Z, Kaminker JS, Hansen DV (2016) Untangling the brain's neuroinflammatory and neurodegenerative transcriptional responses. *Nat Commun* 7:11295.
- Switzer RC 3rd (2000) Application of silver degeneration stains for neurotoxicity testing. *Toxicol Pathol* 28:70–83.
- Switzer RC, Campbell SK, Murdock TM (1993) A histologic method for staining Alzheimer pathology. U.S. Patent 5192688.
- Tee JM, Sartori da Silva MA, Rygiel AM, Muncan V, Bink R, van den Brink GR, van Tijn P, Zivkovic D, Kodach LL, Guardavaccaro D, Diks SH, Peppelenbosch MP (2012) asb11 is a regulator of embryonic and adult regenerative myogenesis. *Stem Cells Dev* 21:3091–3103.
- Tomic JL, Pensalfini A, Head E, Glabe CG (2009) Soluble fibrillar oligomer levels are elevated in Alzheimer's disease brain and correlate with cognitive dysfunction. *Neurobiol Dis* 35:352–358.
- Tsai J, Grutzendler J, Duff K, Gan WB (2004) Fibrillar amyloid deposition leads to local synaptic abnormalities and breakage of neuronal branches. *Nat Neurosci* 7:1181–1183.
- Turnbull IR, Gilfillan S, Cella M, Aoshi T, Miller M, Piccio L, Hernandez M, Colonna M (2006) Cutting edge: TREM-2 attenuates macrophage activation. *J Immunol* 177:3520–3524.
- Ulland TK, Colonna M (2018) TREM2: a key player in microglial biology and Alzheimer disease. *Nat Rev Neurol* 14:667–675.
- Ulland TK, Song WM, Huang SC, Ulrich JD, Sergushichev A, Beatty WL, Loboda AA, Zhou Y, Cairns NJ, Kambal A, Loginicheva E, Gilfillan S, Cella M, Virgin HW, Unanue ER, Wang Y, Artyomov MN, Holtzman DM, Colonna M (2017) TREM2 maintains microglial metabolic fitness in Alzheimer's disease. *Cell* 170:649–663.e13.
- Ulrich JD, Ulland TK, Colonna M, Holtzman DM (2017) Elucidating the role of TREM2 in Alzheimer's disease. *Neuron* 94:237–248.
- Wang A, Das P, Switzer RC 3rd, Golde TE, Jankowsky JL (2011) Robust amyloid clearance in a mouse model of Alzheimer's disease provides novel insights into the mechanism of amyloid-beta immunotherapy. *J Neurosci* 31:4124–4136.
- Wang Y, Cella M, Mallinson K, Ulrich JD, Young KL, Robinette ML, Gilfillan S, Krishnan GM, Sudhakar S, Zinselmeyer BH, Holtzman DM, Cirrito JR,

- Colonna M (2015) TREM2 lipid sensing sustains the microglial response in an Alzheimer's disease model. *Cell* 160:1061–1071.
- Wang Y, Ulland TK, Ulrich JD, Song W, Tzaferis JA, Hole JT, Yuan P, Mahan TE, Shi Y, Gilfillan S, Cella M, Grutzendler J, DeMattos RB, Cirrito JR, Holtzman DM, Colonna M (2016) TREM2-mediated early microglial response limits diffusion and toxicity of amyloid plaques. *J Exp Med* 213:667–675.
- Wu TD, Reeder J, Lawrence M, Becker G, Brauer MJ (2016) GMAP and GSNAP for genomic sequence alignment: enhancements to speed, accuracy, and functionality. *Methods Mol Biol* 1418:283–334.
- Wu T, Dejanovic B, Gandham VD, Gogineni A, Edmonds R, Schauer S, Srinivasan K, Huntley MA, Wang Y, Wang TM, Hedehus M, Barck KH, Stark M, Ngu H, Foreman O, Meilandt WJ, Elstrott J, Chang MC, Hansen DV, Carano RA, et al. (2019) Complement C3 is activated in human AD brain and is required for neurodegeneration in mouse models of amyloidosis and tauopathy. *Cell Rep* 28:2111–2123.e6.
- Wu W, Glinka A, Delius H, Niehrs C (2000) Mutual antagonism between dickkopf1 and dickkopf2 regulates Wnt/beta-catenin signalling. *Curr Biol* 10:1611–1614.
- Yeh FL, Wang Y, Tom I, Gonzalez LC, Sheng M (2016) TREM2 binds to apolipoproteins, including APOE and CLU/APOJ, and thereby facilitates uptake of amyloid-beta by microglia. *Neuron* 91:328–340.
- Yeh FL, Hansen DV, Sheng M (2017) TREM2, microglia, and neurodegenerative diseases. *Trends Mol Med* 23:512–533.
- Yoshiyama Y, Higuchi M, Zhang B, Huang SM, Iwata N, Saido TC, Maeda J, Suhara T, Trojanowski JQ, Lee VM (2007) Synapse loss and microglial activation precede tangles in a P301S tauopathy mouse model. *Neuron* 53:337–351.
- Yuan P, Condello C, Keene CD, Wang Y, Bird TD, Paul SM, Luo W, Colonna M, Baddeley D, Grutzendler J (2016) TREM2 haploinsufficiency in mice and humans impairs the microglia barrier function leading to decreased amyloid compaction and severe axonal dystrophy. *Neuron* 92:252–264.
- Zhao Y, Wu X, Li X, Jiang LL, Gui X, Liu Y, Sun Y, Zhu B, Piña-Crespo JC, Zhang M, Zhang N, Chen X, Bu G, An Z, Huang TY, Xu H (2018) TREM2 is a receptor for beta-amyloid that mediates microglial function. *Neuron* 97:1023–1031.e7.
- Zheng H, Jia L, Liu CC, Rong Z, Zhong L, Yang L, Chen XF, Fryer JD, Wang X, Zhang YW, Xu H, Bu G (2017) TREM2 promotes microglial survival by activating Wnt/beta-catenin pathway. *J Neurosci* 37:1772–1784.
- Zulfiqar S, Tanriöver G (2017) β -Catenin pathway is involved in TREM2-mediated microglial survival. *J Neurosci* 37:7073–7075.